



Turbulence scales for eddy covariance quality control over a tropical dry forest in complex terrain

Eugenia González del Castillo^{a,*}, Kyaw Tha Paw U^b, Arturo Sánchez-Azofeifa^c

^a Graduate Group in Ecology, University of California Davis, 95616 Davis, CA, USA

^b Department of Land, Air and Water Resources, University of California Davis, 95616 Davis, CA, USA

^c Earth and Atmospheric Sciences Department, University of Alberta, Edmonton, AB, T6G 2E3, Canada

ARTICLE INFO

Keywords:

Turbulence scales
Ecosystem fluxes
Carbon dioxide
Net radiation
Energy balance

ABSTRACT

The assessment of the potential for carbon sequestration in tropical dry forests has lagged behind the work done in other tropical environments; the particularities of the carbon dynamics in these ecosystems are largely absent from models of global primary productivity and effects of climate change on vegetation. In Mexico, the largest portions of preserved tropical dry forests have been confined to conservation areas on hilly terrain where productive activities like agriculture are difficult. The location of these remnants of original tropical dry forest in complex terrain presents an operational challenge to directly assess CO₂ exchange between the forest and the atmosphere by means of the eddy covariance (EC) technique. We installed and maintained an EC system over an intact tropical dry forest in the Chamela-Cuixmala Biosphere Reserve in the lowlands of the Pacific Coast of Mexico, to assess the suitability of this technique to measure CO₂ flux, sensible heat and latent heat flux over moderately complex topography in a remote location. The quality of the datasets produced was evaluated through the degree of energy balance closure achieved. Modelling the incoming and outgoing radiation to take into account the slope and aspect of the underlying terrain raised the energy balance closure from 71% to 75%. We also compared the effect of applying three different filters to discriminate conditions of well-developed turbulence: the friction velocity u_* , the standard deviation of the vertical wind σ_w , and two dimensionless indices based on a modified turbulence intensity scale u_{TKE} . u_* and σ_w discriminated fluxes coming from topographically complex areas, according to a flux footprint model, but the filtered subset of data did not showed higher energy balance closure compared to the unfiltered dataset. The u_{TKE} -based filters were more effective screening out periods dominated by horizontal or vertical advective transport instead of turbulence exchange, and raised the slope of the energy balance regression in the filtered data between 3%–17% – depending on the season-, compared to the unfiltered dataset. Together, these procedures of quality assurance and control produced a flux dataset of quality comparable to those obtained in more ideal surfaces.

1. Introduction

Tropical dry forests are ecosystems that, from a potential distribution, cover 47% of all tropical environments. These forests, as defined by Sánchez-Azofeifa et al. (2005), have a mean annual temperature around 25 °C, and a prolonged dry season (less than 100 mm rain per month) that can last from four to six months of the year. During the dry season, 80–100% of plant species are characterized by a deciduous leaf habit. Three well defined phenological seasons can be identified in the vegetation of tropical dry forests: maturity, senescence, and leafless canopy. These phenological events are mostly controlled by soil moisture availability. Tropical dry forests currently have an extension

of about 500,000 km² in the Americas, have high deforestation rates, and their landscape is mostly a combination of agricultural fields and primary and secondary forests (Portillo-Quintero and Sanchez-Azofeifa, 2010). Major threats to their survival are the conversion of the land to pasture for livestock, and the advance of the agricultural frontier where the soil is fertile.

Among the current available carbon flux measurement systems in the FLUXNET database, only 5 of 517 sites are reportedly located in tropical dry forests. In the Americas, two of them are located in the lowlands of the Pacific coast of Mexico: Chamela-Cuixmala Biosphere Reserve, and Tesopaco, Sonora (Pérez-Ruiz et al., 2010) and one more in Costa Rica (Santa Rosa Environmental Monitoring Super Site,

* Corresponding author. Current address: Red Universitaria de Observatorios Atmosféricos, Centro de Ciencias de la Atmósfera, Universidad Nacional Autónoma de México, Circuito Exterior S/N, Ciudad Universitaria, 04510 Coyoacán, Ciudad de México, México.

E-mail address: eu.gonzaranda@atmosfera.unam.mx (E.G. del Castillo).

<https://doi.org/10.1016/j.agrformet.2017.11.014>

Received 9 June 2017; Received in revised form 1 November 2017; Accepted 12 November 2017

Available online 07 December 2017

0168-1923/ © 2017 Elsevier B.V. All rights reserved.

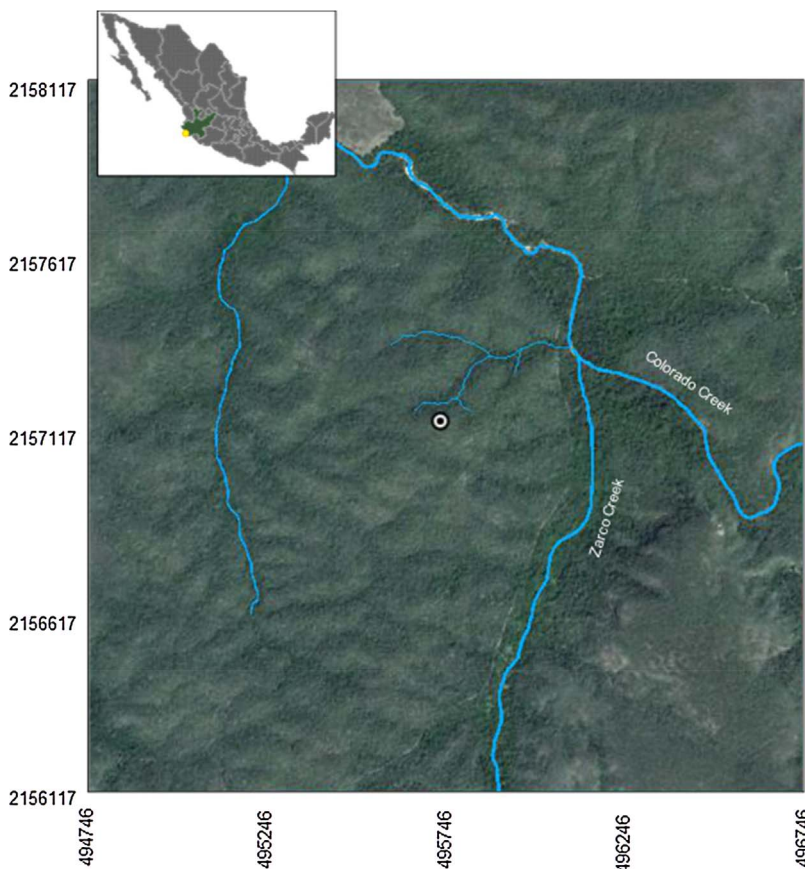


Fig. 1. Location of the Chamela region (yellow dot on insert) in the state of Jalisco (green area on insert), and topographical features of the terrain surrounding the tower (white dot) in an area of 2×2 km. (For interpretation of the references to colour in this figure legend, the reader is referred to the web version of this article.)

Guanacaste). The Chamela-Cuixmala Biosphere Reserve tower operated between 2007 and 2015. These three stations cover a wide annual precipitation range going from 650 mm and 800 mm at the Sonora and Chamela-Cuixmala sites, respectively, to 1445 mm for the Santa Rosa Super Site.

The Chamela-Cuixmala site was situated in a moderately complex topographic terrain and therefore represented a distinct operational challenge. Estimations of carbon sequestration by tropical ecosystems in general have been conducted in relatively flat sites, covered mostly by tropical rainforest, specifically in the Amazon basin (e.g. Mahli et al., 1998; Saleska et al., 2003). In contrast, work on tropical dry forests has lagged behind research done at other tropical ecosystems, in spite of their extension and high deforestation rates (Sánchez-Azofeifa et al., 2005). In Mexico, the most extensive remnants of well-preserved TDF in North and Central America are located in Western coast of Mexico (Ceballos and Garcia 1995; Trejo and Dirzo 2000), in hilly terrain that has not been cleared yet because is not apt for agricultural purposes. Estimates of aboveground biomass increments and CO_2 emissions to the atmosphere during conversion of these forests to other land uses suggest these systems might be sites of substantial CO_2 exchange (Martinez-Yrizar et al., 1996; Kauffman et al., 2003; Jaramillo et al., 2003), however their contribution to the global carbon budget both as intact or secondary forests and as areas subjected to high rates of land use change has only started to receive attention (e.g. Pérez-Ruiz et al., 2010; Verduzco et al., 2015).

With the wider aim to further the understanding of the role that these forests play in the sequestration and storage of CO_2 , here we present an exploration of the suitability of the eddy covariance technique to evaluate the carbon exchange at a tropical dry forest located on moderately complex topography, the type of terrain in which most of the remnants of tropical dry forests of Mexico and the Americas in general persist. Over a flat, homogeneously-covered surface, only the storage and the collective covariance terms of the conservation of mass

species equation must be measured to account for total transport of CO_2 or other scalar, since the horizontal and vertical advection terms are negligible with respect to the magnitude of turbulent transport (e.g. Paw U et al., 2000). Over non-flat terrain, however, both horizontal and vertical gradients of scalar and mean wind velocities develop, not only because the wind follows the terrain, but also because even when the cover is homogeneous, the uneven growth of vegetation over such topography inevitably results in a non-uniform distribution of leaf area, so sources and sinks of C develop within the canopy and produce scalar concentration gradients. The contribution of the mean flow to the total exchange of the scalar in a control volume can no longer be neglected in such conditions, and should be measured or estimated. Advection of CO_2 , water vapor or temperature has proven to be difficult to measure directly in the field, so a lot of research has focused instead on identifying filtering criteria to discriminate periods or conditions of well-developed turbulence, when the advective fluxes to total transport of scalars are relatively negligible. Here we examine the use of three different turbulence scales as indicators of atmospheric conditions when turbulent mixing is adequate. We hypothesize that the effectiveness of each scale to filter out periods when advection dominates can be assessed by evaluating its impact on the energy balance residual (EBR) and closure, and that a dataset of comparable quality to those obtained under more ideal terrain conditions can be constructed by identifying and discarding periods when advective fluxes cannot be ignored. We also hypothesize that over undulating terrain, the available energy for turbulent transport is overestimated if the incoming radiation flux is not corrected to account for the fact that it strikes on sloping surfaces, increasing the estimated energy balance residual. Both the filtering scheme and the radiation correction are applicable to a variety of terrain and vegetated surfaces and need only measurements already available at most eddy covariance study sites.

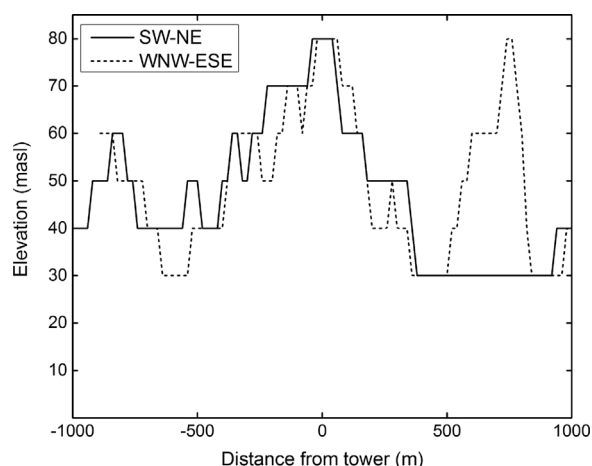


Fig. 2. Elevation profiles for 2-km transects along a SW-NE direction (solid line), and WNW-ESE direction (dotted line), centered at the tower location.

2. Materials and methods

2.1. Site description

The micrometeorological tower used in this study was operational between 2007 and 2015 at the Chamela Biological Station (19°30'34.38"N, 105°02'24.55"W) of the Universidad Nacional Autónoma de México (UNAM), three km inland from the Pacific coastline, in the state of Jalisco, Mexico (Fig. 1). The topography surrounding the tower is characterized by low convex hills with a mean inclination of 12%. An east-facing, steeper range (17% inclination on average) starts 150 m east to the tower, at the bottom of which runs the Zarco creek, a temporary watercourse. There is a second ephemeral watercourse of north-south orientation 600 m to the West of the tower. Two elevation profiles along the most frequent wind directions (SW-NE and WNW-ESE, Fig. 2) show the terrain generally ascends to a low hill of 76 masl where the tower is located. NE to the tower, the topography descends along a gully that joins the riparian zone of the Zarco creek at its bottom. The differences in ground elevation are ameliorated at the canopy surface since the vegetation that grows in the valleys and along ephemeral bed streams is taller than that covering the hillsides and hilltops.

The climate is classified as warm, sub-humid, with a precipitation/temperature coefficient of 31, with summer rains and an isothermal regime (García 1988). Annual temperature averaged 25.7 °C during 1982–2010, according to daily meteorological records kept by the Chamela Biological Station. Mean annual precipitation amounted to 790 mm for the period 1977–2010, with a markedly seasonal distribution as on average less than 10% of the rain fell from November to May. Within the period covered by this study (Nov 2007–Sep 2010) the region experienced a typical water year in 2008, then a moderate El Niño condition prevailed from June 2009 to April 2010 (NOAA Climate Prediction Center, 2016). The warm phase of ENSO is associated with both drier-than-neutral summers and wetter-than-neutral winters in central and southern Mexico (Magaña et al., 2003). At our site, summer precipitation in 2009 was 21% below the historical mean, while winter precipitation (Dec 09–Mar 10) was 3.2 times higher than average.

Hilltops and hillsides are homogeneously covered by undisturbed tropical dry forest, a tree-dominated vegetation characterized by a drought-deciduous leaf habit (Mooney et al., 1995). Canopy height at the tower location is ~10.5 m. Leaf production and shedding is highly seasonal, the Leaf Area Index (LAI) reaches a maximum of 3.2 m² m⁻² and drops to a minimum of 0 m² m⁻² during the dry season (Gonzalez del Castillo et al., in preparation). Leaf flush starts usually in June, a few days after the onset of the rains. Along riparian areas of temporary watercourses, the semi-deciduous tropical forest is the dominant type of

vegetation.

2.2. Micrometeorological measurements

The eddy covariance (EC) system was installed at 12.5 m above ground level (2 m above the canopy) on a steel tower of triangular cross-section. Wind velocity components and sonic temperature were measured at a frequency of 10 Hz with a three dimensional sonic anemometer (CSAT3, Campbell Sci. Inc., Logan, UT, USA) mounted at the end of a 60-cm boom pointing into the direction of the mean wind (240° azimuth). Carbon dioxide and water vapor concentrations were measured at the same frequency using a Li-7500 open-path infrared gas analyzer (IRGA) (Li-Cor Inc., Lincoln, NE, USA). Half-hourly averages of the following meteorological variables were also recorded: air temperature at 6 m height (T107 Campbell Sci. Inc., Logan, UT, USA), temperature and relative humidity at 12.5 m height (HMP45C, Vaisala Oyj, Helsinki, Finland); surface radiometric canopy temperature (4000.4ZL, Everest Interscience Inc., Tucson, AZ, USA) at 13.5 m height, 240° azimuth, and 110° zenith angle; barometric pressure (61205 V, RM Young, Traverse City, MI, USA); net radiation (R_n) at 17 m height (NR-Lite, Kipp and Zonen, Delft, The Netherlands); soil heat flux at 8 cm depth (HFT3, REBS, Seattle, WA, USA); soil temperature 4 cm above the soil heat flux plates and additional soil temperatures at 5, 15, 25 and 40 cm depths (T107 and T101, Campbell Sci. Inc., Logan, UT, USA); and soil volumetric water content at 2.5 cm depth, and vertically integrated over 35–65 cm depth (CS616, Campbell Sci. Inc., Logan, UT, USA). Starting on March 2008, Photosynthetically Active Radiation (PAR) (HOBO S-LIA, Onset Computer Corp., Bourne, MA, USA), incoming (S_{\downarrow}) and reflected (S_{\uparrow}) global solar radiation (300–1100 nm) (HOBO S-LIB pyranometer, Onset Computer Corp., Bourne, MA, USA) were sampled every four minutes at 18 m above ground level and averaged half-hourly. Cumulative precipitation over 30-min periods was recorded at 18 m height with a tipping bucket pluviometer (HOBO SRGB, Onset Computer Corp., Bourne, MA, USA).

Both the high frequency data and the half-hourly means of meteorological measurements were recorded continuously by a CR5000 datalogger (Campbell Sci. Inc., Logan, UT, USA), except for rainfall, PAR, and global solar radiation, which were recorded on a HOBO H21-001 datalogger (Onset Computer Corp., Bourne, MA, USA).

Before the field measurements began, all sensors used were factory calibrated. The gas analyzer was calibrated every six to eight months using soda lime and anhydrous calcium sulfate (drierite) for the zero, and a 1000 ppm CO₂ calibration gas, balance air, for the span.

The micrometeorological tower started operations in November 2007. For the present study, we present results from the starting date through September 2010. There is a large gap in the time series that goes from 25 July, 2008 to 24 January, 2009 due to major failure of the system because of a lightning strike.

2.3. Flux computation and corrections

2.3.1. Turbulent fluxes

The eddy fluxes of CO₂ (F_c), latent heat (LE) and sensible heat (H) were calculated every half hour using the covariance between the high frequency vertical velocity of the wind w and the CO₂ concentration, water vapor concentration and the sonic temperature, respectively. The use of the sonic temperature (which approximates the virtual temperature) instead of air temperature to compute H accounts for the extra thermodynamic energy necessary for a moistened air parcel to expand and decrease its density to achieve constant pressure (Paw U et al., 2000). Accordingly, Schotanus et al. (1983) humidity correction was not applied to the sonic-derived H .

Before flux computation, a modification of the planar fit rotation (Paw U et al., 2000; Wilczak et al., 2001; Yuan et al., 2011; Ono et al., 2008) was applied to the wind field to determine a coordinate frame parallel to the streamline surface. In the planar fit technique, the mean

vertical velocity \bar{w} is estimated as the velocity normal to a plane obtained by multiple regression of the un-rotated vertical velocity against the horizontal components of the wind field. Given the undulating nature of the topography at Chamela, the surface seen by the sensors is wind direction dependent, hence a different plane was fitted for each of 18 sectors with a 20° range each, centered at 0°, 20°, 40°, etc. A separate set of sector-specific rotation planes were fitted for the periods Nov 2007–Jul 2008 and Jan 2009–Sep 2010.

To account for the physical separation between the CSAT3 and the Li-7500, running covariances were calculated over a variable time lag of up to 4 s between w and the scalar of interest ($[\text{CO}_2]$ or $[\text{H}_2\text{O}]$), and the maximum covariance found was then used for flux computations. A correction for the loss of co-spectral power at the high frequency range for the eddy terms of CO_2 and water vapor fluxes was applied using empirical correction factors (CF) based on the sensible heat cospectrum (Aubinet et al., 2000; Gouliden et al., 1996; Su et al., 2004). Although the sensible heat cospectrum derived from the sonic anemometer could exhibit high frequency losses due to the volume averaging effect, it does not suffer from the sensor separation effect or the slower response of the scalar sensors, and therefore it is often used as the standard by which the other fluxes are corrected. Separate CF were calculated for the foliated and leafless seasons of 2009, and for each of nine stability classes that were defined using the parameter $\zeta = z/L$, where z is the measurement height and L is the Obukhov length (Table 1). Finally, CO_2 and water vapor fluxes are adjusted for apparent mass transfer due to variations in density (Webb et al., 1980).

The storage of CO_2 in the air below the EC system is estimated from the half-hourly change in the mean CO_2 concentration at the measurement height (Hollinger et al., 1994), given that no profiling system for CO_2 and temperature within the canopy is installed at the site. The half hourly net ecosystem exchange of CO_2 (NEE) is then calculated as the sum of the storage term and F_c .

2.3.2. Non turbulent fluxes. Net radiation on complex terrain

Starting on March 22, 2008, a modified model for net radiation that takes into account the spatial variation in slope and aspect of the terrain surrounding the tower was implemented.

The net radiation received by any surface is given by the balance between incoming ($S\downarrow$) and outgoing ($S\uparrow$) shortwave radiation, and incoming ($L\downarrow$) and outgoing ($L\uparrow$) longwave radiation (Eq. (1)):

$$R_n = S\downarrow + S\uparrow + L\downarrow + L\uparrow \quad (1)$$

We follow here the convention that assigns negative signs to upward radiation flux terms and positive signs to downward fluxes.

Over sloping or complex topography, the evaluation of the terms in Eq. (1) is considerably more complicated than over a horizontal flat surface. The net radiation budget should ideally be measured parallel to the tilted surface, however, the radiation measurements are typically

done with horizontally leveled instruments, and the measurements later rotated into a surface-parallel frame. Here we will assume that long-wave radiation is isotropic, thus will not be rotated. This way, only the shortwave radiation components are functions of the slope and orientation of the surface relative to the incoming solar beam. These assumptions are supported by the results of Whiteman et al. (1989) and Holst et al. (2005) among others, when comparing observations from tilted and horizontal sensors.

For a horizontal surface, $S_{H\downarrow}$ (where the subindex H stands for horizontal) is composed by a direct beam fraction (S_{bH}) and a diffuse fraction (S_{dH}) that comes mainly from the scattering of solar radiation by the sky (Eq. (2)):

$$S_{H\downarrow} = S_{bH} + S_{dH} \quad (2)$$

whereas over tilted or complex terrain (subindex β), $S_{\beta\downarrow}$ should further include radiation reflected from the adjacent topography ($S_{r\beta}$) (Eq. (3)):

$$S_{\beta\downarrow} = S_{b\beta} + S_{d\beta} + S_{r\beta} \quad (3)$$

$S_{r\beta}$ is ultimately irrelevant to our model since the radiation measurements are done at the top of an elevated portion of the land, where the tower is located, and thus the reflection from adjacent areas does not reach the upward pyranometer.

In order to partition $S_{H\downarrow}$ into its direct and diffuse components, we computed a half-hourly clearness index k_T (Eq. (4)), the ratio of the measured $S_{H\downarrow}$ at the surface to the modeled global solar radiation incident on a horizontal surface outside the atmosphere S_o (Eq. (5)) (Duffie and Beckman, 2006).

$$k_T = \frac{S_{H\downarrow}}{S_o} \quad (4)$$

$$S_o = SC(1.00011 + 0.034221 \cos B + 0.001280 \sin B + 0.000719 \cos 2B + 0.000077 \sin 2B) \cos \theta_z \quad (5)$$

where SC is the solar constant (1367 W m^{-2}), B accounts for the dependence of the extraterrestrial radiation on the elliptical orbital position as indicated by the day of year (DOY) (Eq. (6)), and the cosine of the solar zenithal angle (θ_z) is a function of the location's latitude (ϕ), the solar declination (δ) and the hour angle (ω) (Eq. (7)).

$$B = (\text{DOY} - 1) \frac{360}{365} \quad (6)$$

$$\cos \theta_z = \cos \phi \cos \delta \cos \omega + \sin \phi \sin \delta \quad (7)$$

Solar position angles δ and ω were calculated using NOAA's Solar Calculator spreadsheet (NOAA ESRL, 2016) based on astronomical algorithms (Meeus, 1998).

A parameterization by Erbs et al. (1982) that correlates k_T to the

Table 1

Cospectral correction factors (CF) for high frequency losses of CO_2 and water vapor fluxes by stability class at the Chamela site. The determination coefficient (R^2) of the linear least-square fit for an empirical transfer function by stability class and the number of half hours used (N) are also given. Dashes indicate that no CF was computed due to large variability in the regression parameters of the transfer function.

Stability	Leafless (May-June 2009)		Water vapor		N	Foliated (July 2009)		Water vapor		N
	CF	R^2	CF	R^2		CF	R^2	CF	R^2	
$\zeta > 0.1$	1.02	0.81	1.04	0.50	84	–	–	–	–	–
$0.0 < \zeta \leq 0.1$	1.03	0.91	–	–	58	–	–	–	–	–
$-0.1 < \zeta \leq 0.0$	1.02	0.98	1.01	0.68	190	1.023	0.97	1.113	0.86	120
$-0.2 < \zeta \leq -0.1$	1.02	0.98	1.03	0.23	173	1.018	0.98	1.018	0.91	133
$-0.3 < \zeta \leq -0.2$	1.02	0.98	–	–	88	1.014	0.98	1.021	0.80	50
$-0.4 < \zeta \leq -0.3$	1.02	0.98	1.01	0.47	34	1.016	0.96	1.037	0.95	16
$-0.5 < \zeta \leq -0.4$	1.00	0.89	–	–	13	1.013	0.92	1.028	0.96	7
$-1.0 < \zeta \leq -0.5$	1.01	0.96	1.00	0.47	26	1.012	0.94	1.028	0.88	22
$-1.0 \geq \zeta$	1.01	0.86	–	–	29	1.015	0.66	1.035	0.53	20

ratio of the diffuse component to the global solar radiation ($S_{dH}/S_{H\downarrow}$) was used to obtain S_{dH} (Eq. (8)), and by difference, the direct beam component S_{bH} .

$$\frac{S_{dH}}{S_{H\downarrow}} = \begin{cases} 1.0 - 0.09 k_T & \text{for } k_T \leq 0.22 \\ 0.9511 - 0.1604 k_T + 4.388 k_T^2 - 16.638 k_T^3 + 12.336 k_T^4 & \text{for } 0.22 < k_T \leq 0.80 \\ 0.165 & \text{for } k_T > 0.80 \end{cases} \quad (8)$$

The beam radiation S_{bH} was then rotated every half hour into a slope-parallel coordinate system to yield the beam radiation over the tilted surface ($S_{b\beta}$). The rotation factor is the quotient between the cosine of θ_i , the angle between a vector pointing towards the sun and a vector normal to the tilted surface, and the cosine of θ_z (Eq. (9)–(10)).

$$S_{b\beta} = S_{bH} \frac{\cos \theta_i}{\cos \theta_z} \quad (9)$$

$$\cos \theta_i = \sin \delta \sin \phi \cos \beta - \sin \delta \cos \phi \sin \beta \cos \alpha + \cos \delta \cos \phi \cos \beta \cos \omega + \cos \delta \sin \phi \sin \beta \cos \alpha \cos \omega + \cos \delta \sin \beta \sin \alpha \sin \omega \quad (10)$$

where β is the slope angle of the surface with respect to the horizontal (dip), and α the surface azimuth angle (aspect-perpendicular to the strike), measured clockwise with zero due South. In contrast to a uniformly tilted terrain, the complex topography surrounding the tower at Chamela cannot be characterized by a single slope and aspect. Therefore, from a 10 m resolution Digital Elevation Model of the site, we derived β and α angles for 900 points situated at the vertices of a square grid in a 170-m radius circle centered on the tower, with each point being 10 m away from its nearest neighboring point. The size of the circle was chosen to match the area seen by the NR-Lite radiometer at 17 m height. The beam component of the incident radiation was computed using Eqs. (9)–(10) at each point, and then averaged across the grid to yield a mean $S_{b\beta}$ for each half hour. The 10-m contour lines were extracted with photogrammetric techniques from stereoscopic pairs of aerial photographs of the Reserve (Cotler et al., 2002). The digitized contour lines were then transformed to the digital raster surface used in this study by Dr. Miguel Ortega (Institute of Biology, UNAM) (Ortega M., personal communication).

The diffuse radiation over the sloping surface $S_{d\beta}$ (Eq. (11)) was also calculated from its horizontal counterpart (Liu and Jordan, 1962) for each point in the grid, and then averaged spatially across points each half hour.

$$S_{d\beta} = S_{dH} \left(\frac{1 + \cos \beta}{2} \right) \quad (11)$$

The models for the diffuse term in Eq. (11) presume an isotropic distribution of the intensity of the radiation coming from the sky (Hay, 1993). This isotropic sky assumption has been challenged by many (e.g. Temps and Coulson, 1977; Perez et al., 1987), but will prevail in this study for simplicity. Matzinger et al. (2003) among others discuss empirical evidence of anisotropic diffuse reflection and its effect on slope-parallel vs. horizontal radiation measurements for points located on the hillsides or valleys in a mountainous region.

Finally, the radiation received by the complex terrain R_{nS} was calculated as (Eq. (12)):

$$R_{nS} = R_{nH} - S_{H\downarrow} + S_{\beta\downarrow} \quad (12)$$

Following Younes et al. (2005), the net radiation components were not rotated if: 1) the solar elevation was lower than 7° , 2) k_T fell outside the range $0 < k_T < 1$, or 3) the diffuse radiation to global radiation ratio $S_{dH}/S_{H\downarrow}$ was outside the limits $0 < S_{dH}/S_{H\downarrow} < 1$.

2.3.3. Non turbulent fluxes. Soil heat flux and storage terms

Soil heat flux density at the surface (G) was calculated as the

average of the heat plates output corrected for the change in the heat stored in the layer above them, obtained from the half hourly change in soil temperature from the thermocouples situated above the flux plates (McCaughey and Saxton, 1988).

The thermal energy stored in the biomass (S_v) below the EC system was estimated using Eq. (13) (Samson and Lemeur, 2001):

$$S_v = c_v m_v \frac{\Delta T_v}{\Delta t} \quad (13)$$

where c_v , the specific heat of vegetation, was assumed to be $2930 \text{ J kg}^{-1} \text{ }^\circ\text{C}^{-1}$ (Thom, 1975), m_v is the vegetation density at the site (8.5 kg m^{-2}) estimated by Martinez-Yrizar et al. (1992) by harvesting all plants of at least 3.0 cm in diameter in 40 plots ($5 \text{ m} \times 5 \text{ m}$) close to the location of the tower, measuring their height and total fresh mass and then drying subsamples of boles, stems and branches to a constant mass at 105°C , ΔT_v is the half-hourly change in vegetation temperature, and Δt is the time step (1800s). We did not measure the change in temperature in the different elements of the vegetation, so we approximated ΔT_v with the air temperature change measured at 6 m height for the lower half of the canopy, and with the radiometric surface temperature for the upper half.

The storage of sensible (S_a) and latent heat (S_w) in the air column below the net radiometer height were calculated as (Eqs. (14) and (15)):

$$S_a = \rho c_p \sum_{i=1}^n \frac{\Delta T_a}{\Delta t} \Delta z_i \quad (14)$$

$$S_w = \rho_d \lambda \sum_{i=1}^n \frac{\Delta \chi_w}{\Delta t} \Delta z_i \quad (15)$$

where c_p is the specific heat capacity of air, ρ is the density of moist air, ΔT_a is the change in air temperature at each measurement height z_i , ρ_d is the density of dry air, λ is the latent heat of vaporization, and χ_w is the mixing ratio of water vapor in dry air (McCaughey and Saxton, 1988). Since we measured air temperature at only two heights, the time-step change in temperature at 6 m was taken as representative of that of the bottom 8.5 m of the air column, and the change in temperature measured at 12.5 m was considered to represent that of the upper half. The water vapor in the air column was measured only at 12.5 m height, and its change was taken to be representative of the whole column.

2.4. Data filtering and quality control

Turbulent fluxes were excluded from further analysis if one or more of the following criteria were met: 1) precipitation occurred during the measurement, 2) diagnostic flags either from the anemometer or the IRGA indicated an invalid data point, 3) other instrument failure took place, and 4) data showed physically implausible values.

2.4.1. Turbulence intensity indices

With the aim of identifying and discarding fluxes measured under inadequate low turbulent mixing conditions, three different indicators of turbulence strength were used and compared: 1) a modified turbulence intensity scale u_{TKE} (Wharton et al., 2009), 2) the surface friction velocity u_* (e.g. Goulden et al., 1996; Aubinet et al., 2000; Gu et al., 2005), and 3) the standard deviation of vertical wind velocity σ_w (Acevedo et al., 2009).

The turbulence intensity scale u_{TKE} is defined as (Eq. (16)):

$$u_{TKE} = \sqrt{\overline{u'^2} + \overline{v'^2} + \overline{w'^2}} = \sqrt{2TKE} \quad (16)$$

where $\overline{u'^2}$, $\overline{v'^2}$, and $\overline{w'^2}$ are the variances of the horizontal (u), cross-wind (v), and vertical (w) wind velocities. The use of u_{TKE} assumes that the magnitude of the turbulent kinetic energy (TKE) of the flow controls the efficiency of turbulence to transport mass and energy. In order to identify the conditions under which a significant contribution of

advective transport of a scalar occurred, two dimensionless turbulent intensity indices I_u and I_w were derived. The indices are based on the ratio between the mean horizontal (\bar{U}) and an estimated vertical (\bar{w}_{plane}) wind velocities to u_{TKE} (Wharton et al., 2009) (Eqs. (16) and (17)):

$$I_u \equiv \frac{\bar{U}}{u_{TKE}} \quad (17)$$

$$I_w \equiv \frac{\bar{w}_{plane}}{u_{TKE}} \quad (18)$$

I_u and I_w provide a simple approach to determine the periods when transport by mean flow dominates over turbulent transport, and therefore horizontal and vertical advection can no longer be neglected, based on theoretical considerations (see Park and Paw U, 2004, and Kochendorfer et al., 2011). More complex dimensionless analysis points to the ratio of turbulent exchange to mean advective exchange being related to the dimensionless number (Eq. (19)),

$$\frac{xK}{uh^2} \quad (19)$$

where x is the upwind fetch, h is the canopy height, K is a turbulent transport coefficient that should be directly dependent on a turbulent characteristic velocity scale such as u_{TKE} , and u is the mean horizontal wind speed (Park and Paw U, 2004). Therefore for any particular tower with an ecosystem height and fetch, the dimensionless turbulent indices I_u and I_w are inversely proportional to the dimensionless number defined by Park and Paw U (2004) and they should be related to the proportion of the total exchange that an eddy-covariance system can measure.

\bar{w}_{plane} is estimated through multiple regression of the measured \bar{w} on the mean horizontal components of wind velocity (Eq. (20)) (Paw U et al., 2000; Wilczak et al., 2001):

$$\bar{w}_{plane} = b_0 + b_1 \bar{u} + b_2 \bar{v} \quad (20)$$

where b_0 , b_1 and b_2 are the sector-specific multiple regression coefficients of the planar fit rotation.

A critical value for each measure of turbulence strength was determined visually by inspecting a scatterplot of NEE versus a given filter for both daytime and nighttime. The threshold was selected as the filter value where NEE started to level off. Beyond such threshold no further increment of the turbulence intensity (i.e. a reduction of the absolute magnitude of the u_{TKE} -based indices, or an increment of u_* or σ_w) results in higher absolute carbon fluxes. The filtering processes assume that the release and consumption of carbon via photosynthesis and respiration are independent from the intensity of turbulence. Rather than a decline in biological activity, a reduction of NEE under low turbulence implies the effect of two concepts: 1) poor mixing conditions in the atmosphere, so exchange was through mean advection rather than turbulent transport, and 2) the inability of the instruments to sense weak, small scale turbulence. Half hourly data identified as affected by low turbulent transport under each criterion were flagged and discarded.

The effectiveness of each filtering technique was compared by examining 1) its effect on the energy balance closure for the site, 2) its impact on the response of the resulting NEE datasets to two independent controlling variables: PAR and soil moisture, and 3) the spatial relationship of the data both within and outside the critical thresholds to the topographical features of the site via the estimation of their footprint.

2.5. Footprint calculations

The influence of the topography on the measured fluxes was assessed via a parameterized footprint model developed by Kljun et al. (2004). Although we recognize that this model does not treat the details of turbulent transfer within forest canopies, it is used as a standard for general footprint analysis over ecosystems (e.g. Barcza et al., 2009;

Hopkinson et al., 2016; van Gorsel et al., 2013). For each half hour we calculated the cross-wind integrated contribution \bar{f}^y and the upwind distance x_R from the tower at which a cumulative percentage R of the source area was reached, where R went from 5 to 90% every 5%. The estimations of \bar{f}^y were aggregated over 10×10 m cells, in a square grid (0.25 km^2) centered on the tower. The aggregation was done separately for the datasets within and outside the thresholds of the three turbulence scales.

The inputs needed for the model are the flux measurement height z_m , the surface friction velocity u_* , the standard deviation of the vertical wind velocity σ_w , and the roughness length z_0 ($z_0 = 1.0$ for the Chamela forest). Kljun et al. (2004) parameterization is found to be valid within moderate values of surface friction velocity ($u_* \geq 0.2 \text{ m s}^{-1}$) and for a limited range of boundary layer stability conditions ($-200 \leq z_m/L \leq 1$, where L is Obukhov's length). For the model runs, we adhered strictly to the stability constraint but obtained footprint estimations for both limited and relaxed u_* ranges. We acknowledge that the validity of the footprint estimates for $u_* < 0.2 \text{ m s}^{-1}$ is questionable, but the shift in size and location under such conditions affects the whole flux dataset before the turbulence filters are applied, and therefore would not bias the comparison of the discriminating power for low mixing conditions between them.

To evaluate the turbulence scales ability to filter out fluxes from topographically challenging areas, we constructed a measure of wind trajectory complexity L_t , for all possible wind directions towards the tower in a 500 m-radius circle (Eq. (21)), which is related to a simplistic way to describe an aspect of fractal analysis:

$$L_t \equiv \frac{l_{terrain}}{l_{straight}} \quad (21)$$

where $l_{terrain}$ is the length of a segmented line that follows the elevation variations of the terrain starting at the tower and upwind to a certain end point, and $l_{straight}$ is the length of the straight line connecting the tower location with the same end point. By definition, $L_t = 1$ for a line that intersected only flat terrain, while a value for wind trajectory complexity of, for example $L_t = 1.15$ would describe a pathway that is 15% longer at ground level compared to a straight line between its ending points. L_t was computed every 10 m starting at the tower and up to a distance of 500 m away from it for 360 wind trajectories 1° apart from each other (Fig. 3). Finally, we associated a characteristic L_t to the wind trajectory of every single half hour of flux measurements, taking $l_{straight} = x_{90}$, and the fraction of periods that fell outside the critical values for each turbulence scale was computed for every L_t decile.

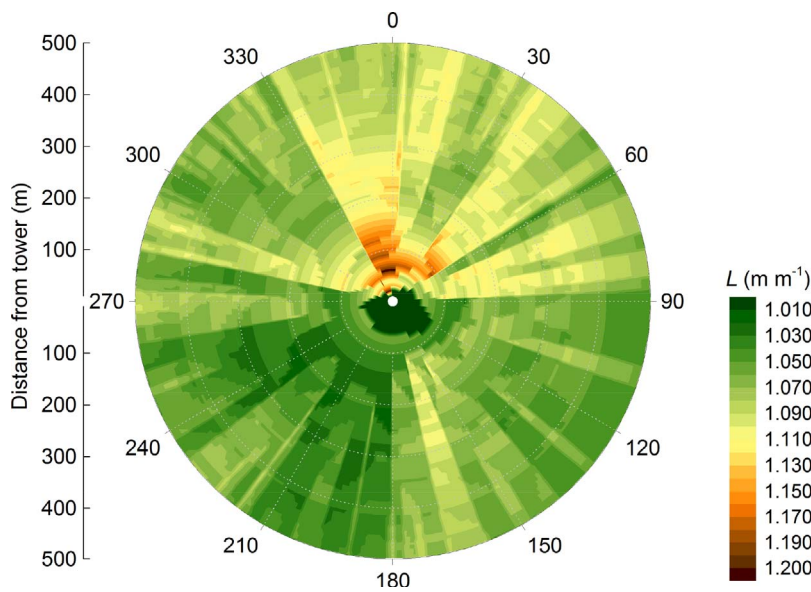
3. Results and discussion

After discarding unusable periods due to power outages, instrument failure, calibration or maintenance, rain and fog, a total of 26,133 half hours (62% of total) were available for the analysis. While periods affected by rain were relatively scarce (less than 1% of the time), foggy conditions occurred frequently at the site, particularly early in the morning (7 am to 9 am).

3.1. Wind speed and direction

The wind field at the study site exhibits the bimodal distribution of wind directions that is typical of a sea-land breeze pattern of a coastal location (Fig. 4). Daytime average wind speed is 2.7 m s^{-1} and 61% of the time comes from the 220° to 310° sector. The 125° – 215° sector comprises an additional 16% of daytime wind directions. Noticeably, wind coming from this sector has an average speed higher than 4 m s^{-1} during 42% of daytime compared to 24% in all other directions. Average wind speed reaches a maximum of 3.6 m s^{-1} between 1230 and 1630 h, mostly from the West (233° – 300°). The direction then changes to the NW quadrant and the wind speed decreases. In the hour

Fig. 3. Terrain complexity for 360 wind directions, 1° apart, in a circle of 500 m radius centered on the tower.



following dusk, wind direction transitions to the NE. During nighttime and up to 0900 h, mean wind speed is 1.3 m s^{-1} and the wind predominantly comes from the NE, as 67% of nighttime wind directions are from the 20° – 90° sector. Overall, low wind speed ($\leq 2.0 \text{ m s}^{-1}$) characterizes 83% of half hours at night. Around 0830–0900 h, the wind reaches a minimum average speed of 1.1 m s^{-1} and within the next hour turns back to the SW sector, traversing predominantly across the NW quadrant.

3.2. Turbulence intensity scales

The daily courses of the mean wind speed and the various turbulence intensity indicators used in this study, along with the atmospheric stability parameter z/L are illustrated in Fig. 5. The average wind speed U shows an asymmetrical daily pattern. At sunrise, as the atmosphere turns unstable, U drops from its nighttime values and reaches a minimum around 0900 h, then rises quickly to its peak at 1400 h and comes back to its nighttime level around 2030 h. Friction velocity u^* rises more slowly and reaches its peak value at 1500 h, while both u_{TKE} and σ_w peak at 1400 h. All three turbulence scales u_{TKE} , u^* and σ_w show broad peaks, staying within 90% of their maximum value for at least four hours. They also exhibit a more symmetrical pattern than U . Whereas none of the turbulence scales on the top panel in Fig. 3 display

a drop in intensity at sunrise, I_u does capture the changes in the mean wind speed with increasing instability, reaching a minimum –i.e. greatest turbulence intensity– at the time of maximum atmospheric instability around 0930 h. I_w stays positive from 0900 h to 2130 h, signaling the dominance of the thermally-induced turbulence during the day.

3.3. Energy balance

3.3.1. Spectral corrections

The spectral correction factors for CO_2 fluxes range from 0.2 to 3% during the leafless season and from 1 to 2% during the foliated season (Table 1). The attenuation for water vapor flux spans a larger range, averaging 1–4% during the leafless season, and 2–11% in the foliated period. These corrections are small and well within the range reported for open-path gas analyzers by Massman (2000) and Haslwanter et al. (2009).

3.3.2. Effect of net radiation model for sloping terrain

We evaluated the effect of correcting the net radiation flux to account for the complex topography on the energy balance residual (EBR) and closure. The EBR is the difference between the available energy ($R_n - G - S_v$) and the energy dissipated via turbulent fluxes ($H + LE$). Wind

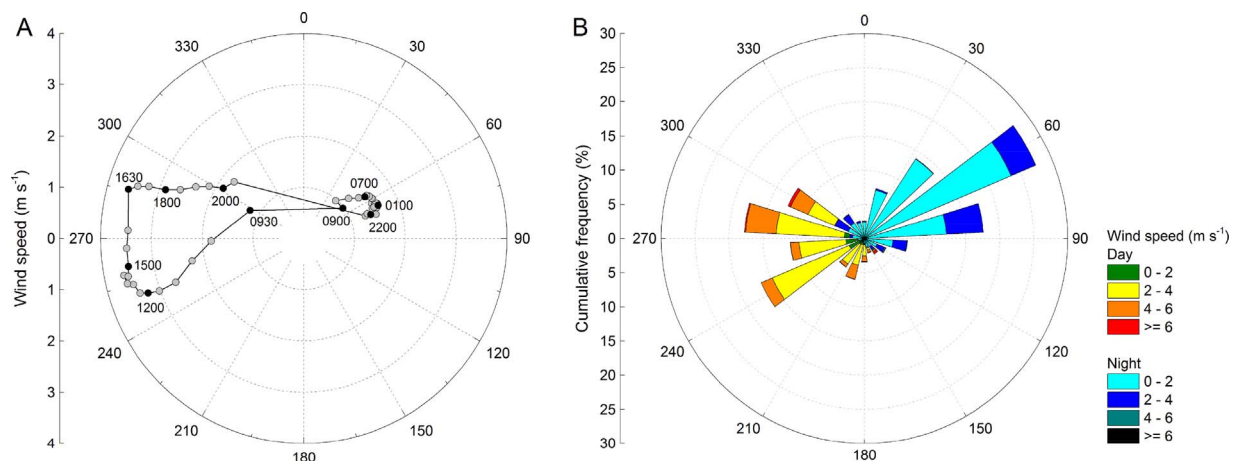


Fig. 4. (A) Daily course of average wind speed and most frequent wind direction over 30-min periods. (B) Wind rose for daytime and nighttime periods at the Chamela site. Frequencies are cumulative and computed over 20° bins; colors represent wind speed classes.

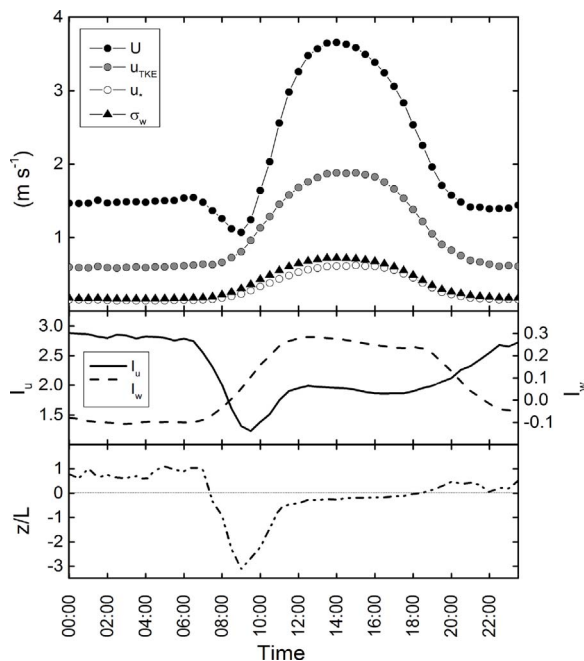


Fig. 5. Top: average daily course of wind speed U , surface friction velocity u_* , standard deviation of vertical wind velocity σ_w and the turbulence intensity scale u_{TKE} at Chamela. Middle: the mean daily evolution of the u_{TKE} -based turbulence indices I_u and I_w . Bottom: average daily course of the stability parameter z/L .

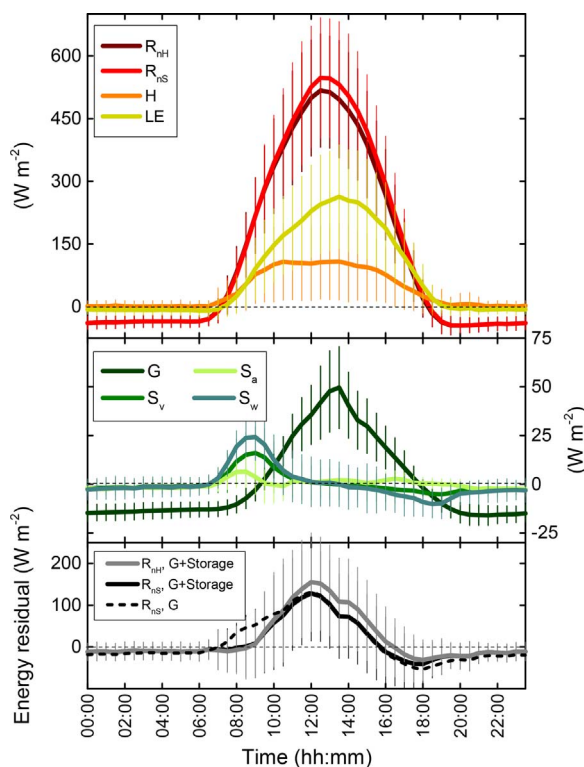


Fig. 6. Top: average daily course of net radiation incident on a horizontal surface (R_{nH}) and complex terrain (R_{nS}), sensible heat (H), and latent heat (LE) flux at Chamela. Middle: Soil heat flux (G), sensible (S_a) and latent (S_v) heat stored in the air column and in the vegetation (S_v). Bottom: average daily course of the energy balance residual once all turbulent flux terms ($H+LE$), G and all storage terms have been subtracted from net radiation ($R_{nH} G+Storage$, and $R_{nS} G+Storage$) or the storage terms have been ignored ($R_{nS} G$). Error bars are 1SD.

direction, fetch, and the digital elevation map analysis described earlier were used to categorize the upwind topography. Compared to the flat surface case, the incident radiant flux and the EBR over the hilly terrain are slightly larger ($1\text{--}6 \text{ W m}^{-2}$) from 0700 to 0900 h; for the rest of the day (0930–1900 h) they both are reduced by 19 W m^{-2} on average (Fig. 6). As the EBR approaches zero around 1600–1630 h for the flat surface condition, the reduction in radiation incident over the complex surface is not accompanied by a similar reduction in sensible and latent heat fluxes, so the energy closure gap actually widens slightly from 1600 to 1800 h for the sloping terrain condition. At nighttime, the differences are negligible. Overall, the estimated slope (\pm SE) of the regression of the turbulent fluxes against the available energy (the energy budget closure) was 0.71 ± 0.00 before the net radiation correction and improves to 0.75 ± 0.00 afterwards.

An incomplete accounting of the sensible and latent heat stored in the moist air column below the net radiometer and within the biomass, has demonstrated to contribute significantly to the energy imbalance that characterizes most flux studies (e.g. Oliphant et al., 2004; Leuning et al., 2012). At our site, a proper measurement of the storage terms was precluded by the lack of instrumentation; nevertheless, we found that even our crude estimation of the thermal storage systematically lowered the energy budget residual from 0730 to 1330 h (Fig. 6) by an average of $2\text{--}45 \text{ W m}^{-2}$. The use of the radiometric surface temperature and air temperature to evaluate the heat stored in the biomass is sufficient only in the case of small-statured and non-woody vegetation, like grasses and crops, but it is not suitable for measuring the heat transfer across boles and branches of large trees (Leuning et al., 2012). Given that more than 50% of the trees at Chamela have a diameter smaller than 8 cm, the underestimation of the heat stored at the biomass is likely not as severe at our site as could be in taller, more massive forests. However, the daily march of the EBR after all storage terms have been subtracted from the available energy, still suggests that we do not account for all thermal storage in the air and the vegetation, because the residual peaks 30 min–1 h before the available energy does, and becomes negative 2–3 h before sunset (Fig. 6).

3.3.3. Effect of low turbulence filtering

Scatterplots of NEE against each turbulence scale are presented in Fig. 7 for both day and night periods and for all available data; also shown are mean NEE by filter binned into half-decade classes of turbulence intensity (Fig. 8). In general, NEE increases with turbulence (i.e. as I_u and $|I_w|$ decrease, and u_* and σ_w increase) up to a threshold beyond which no further increment of NEE is observed. At nighttime, mean NEE slightly drops at the highest turbulence class for both u_* and σ_w filters. The apparent large reduction in NEE with turbulence intensity at nighttime for I_u , u_* and σ_w in the scatterplots is likely a graphical artifact due to the scarce number of measurements under high turbulence. For low to medium turbulence levels, low NEE data points are numerous but most of them are hidden in the plot. Fig. 8 shows that when data are binned into half-decade classes of turbulence indicator so the tendency of NEE among turbulence conditions can be fairly compared, the carbon exchange rises steadily with increasing turbulence, and only the last NEE data point falls slightly. During daytime, NEE also shows a small reduction at the highest portion of the turbulence intensity range for I_u , u_* and σ_w , a tendency previously noticed for u_* by other authors at nighttime only (e.g. Turnipseed et al., 2002; Barr et al., 2006). Such a reduction, however, is likely not significant; we did not perform statistical comparisons between NEE means between turbulence classes, but a visual inspection of the error bars of the mean for the highest turbulence class in Fig. 8A–B and E–I suggests these last points are not different from their immediate neighbors.

For I_w , we do observe that absolute NEE does not peak at $I_w = 0$ during daytime, which results from the fact that the application of a planar fit to the data finds a plane parallel to the tilted surface for which the wind vertical velocities average zero for the entire dataset. The quantity w_{plane} used in the formulation of I_w falls along this plane, and is

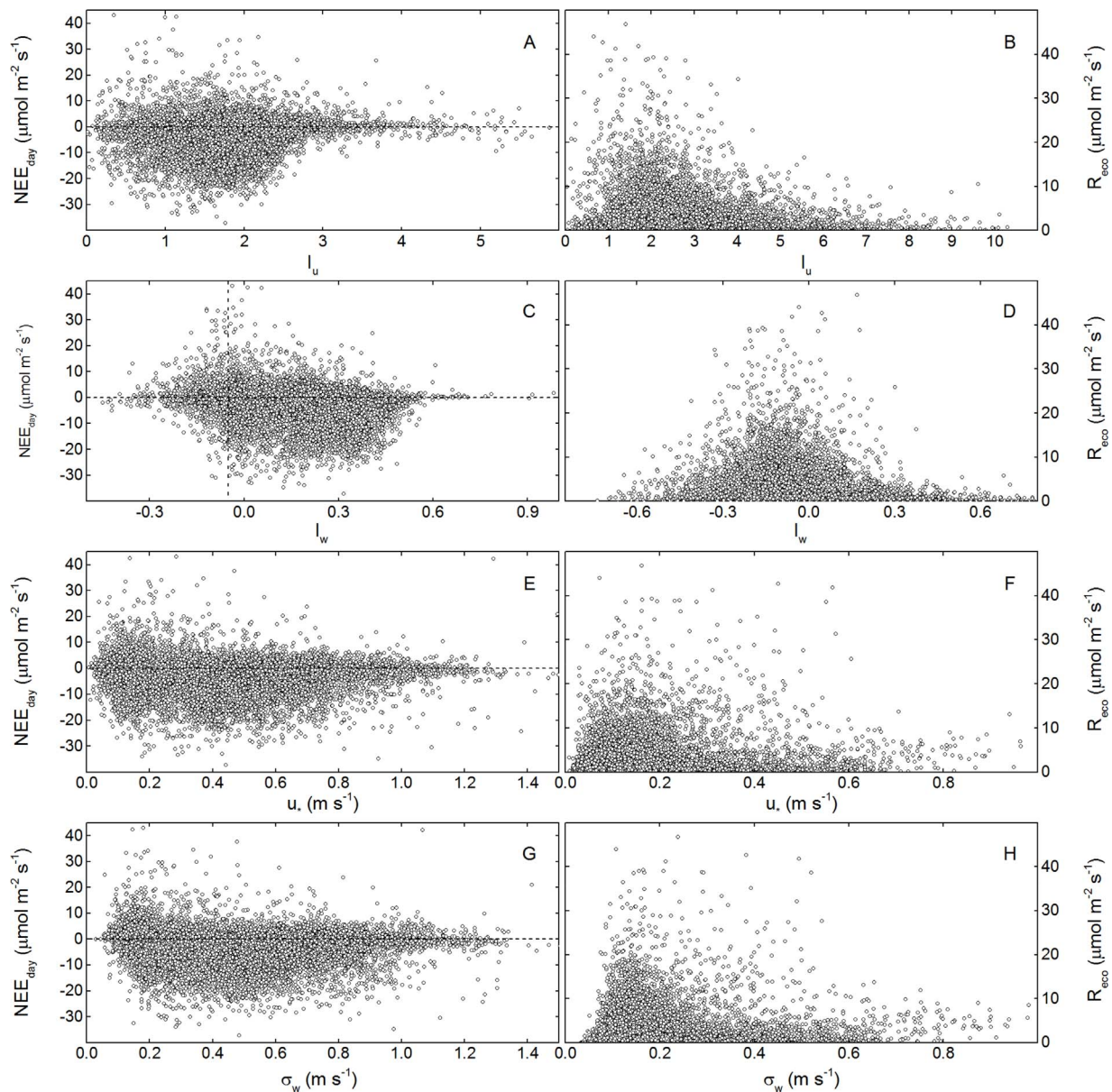


Fig. 7. Net ecosystem exchange (NEE) during daytime (left panels) and nighttime ecosystem respiration (R_{eco} ; right panels) in relation to the scale of horizontal advection to turbulence intensity ratio I_u (A,B), the vertical advection to turbulence intensity ratio I_w (C, D), the surface friction velocity u_* (E, F), and the standard deviation of the vertical wind velocity σ_w (G, H).

not necessarily equal to 0 for every 30-min period. That a larger portion of the cloud of points show a positive sign likely reflects the general upward motion of the flow towards the tower, following the terrain.

Although all available data are plotted against each turbulence scale in Fig. 7, the critical values for identification of advection-affected fluxes were determined separately for three phenological stages on each annual cycle: 1) growth period, which comprises leaf flushing and maturity, 2) senescence, and 3) leafless canopy (Table 2). Such stages roughly correspond to the rainy season, early dry season and late dry season, respectively. Besides the typical water years (June–May) of 2008 and 2010 and their associated phenophases, an additional – albeit shorter – phenological cycle of green-up, maturity and senescence was brought by the rains in winter 2010. In the tropical dry forest, both daytime NEE and nighttime R_{eco} are positively correlated with soil water content, thus pooling together measurements made during dry and wet periods could bias the screening procedure in favor of observations made during the rainy season (Gu et al., 2005).

The critical values found for each turbulent indicator and the

percentage of half hours retained after elimination of data affected by poor mixing are summarized in Table 2. The amount of available data retained by the use of u_* is 8–67% higher compared to I_u – I_w during the day. σ_w identifies 17–66% more data as acceptable than I_u – I_w at daytime. At night, usage of the u_* filter allows retention of 2–48% more periods compared to I_u – I_w except for the two growth periods in 2010, while σ_w retains 9–57% more half hours than I_u – I_w , but not for the senescing canopy of 2007–2008 and the winter growth of 2010.

The exclusion of data affected by the poor mixing conditions identified by each filter impacted the energy budget closure differently for each phenophase (Table 3). Before screening out the advection-affected data (but after applying the radiation correction), sensible and latent heat flux underestimated the available energy by as much as 28% for the senescing canopy after the winter rains in 2010, but only by 17% in the senescence after the summer rains of 2009. On average, our site is situated in the mid to low portion of the closure achieved by 50 FLUXNET site-years examined by Wilson et al. (2002) (mean slope of 0.79 ± 0.01 , range 0.50–0.99). Excluding the senescent canopy of

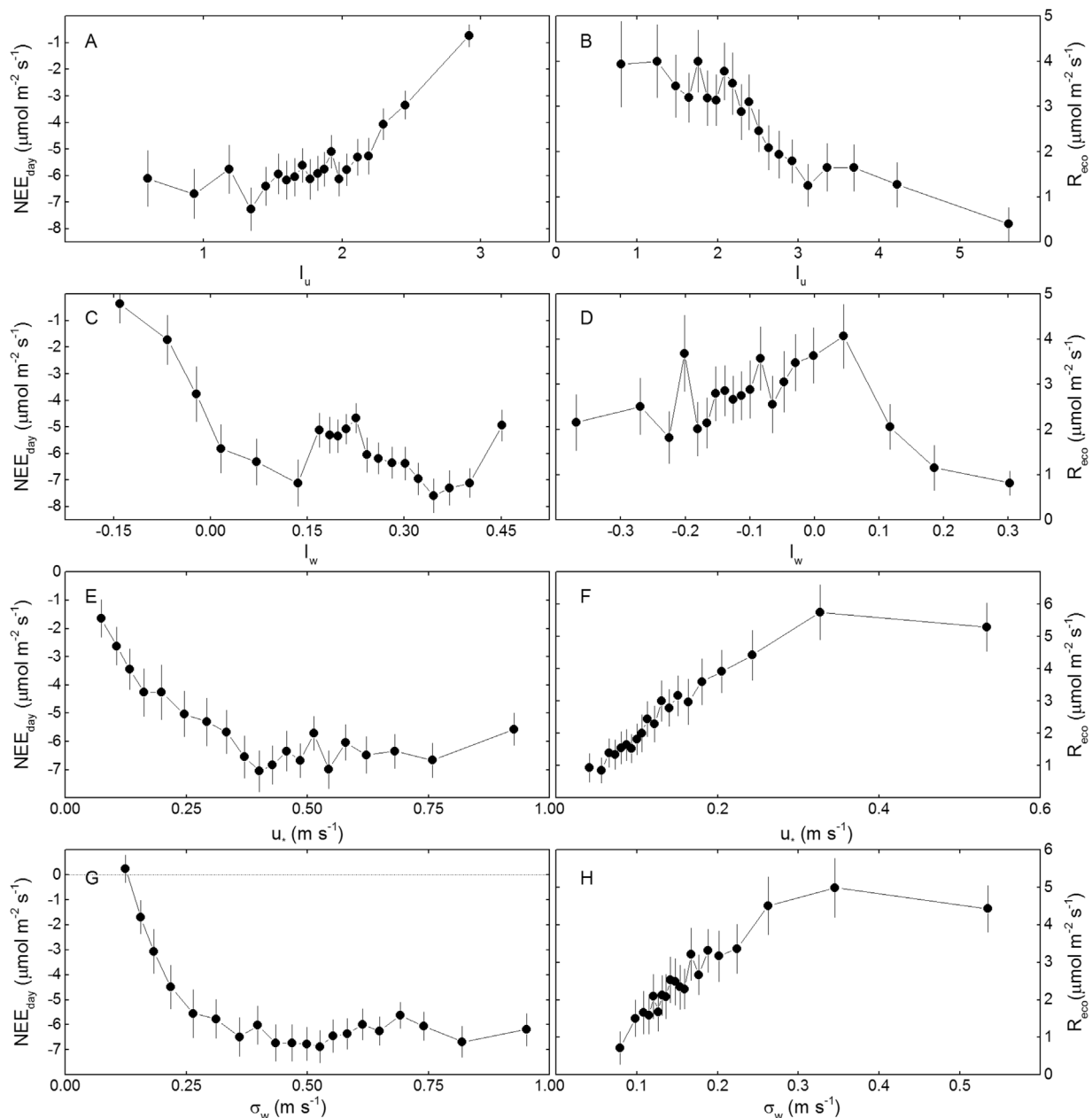


Fig. 8. Average Net ecosystem Exchange (NEE) by turbulence filter binned into half-decade classes of turbulence intensity at daytime (A, C, E, G) and nighttime (B, D, F and H). Error bars are standard errors of the NEE mean.

2007–2008 for which the radiation correction was not applied, the combined use of I_u and I_w consistently raised the slope of the EB equation by a modest 7% on average (range 3–10%). In contrast, for all phenophases considered, the lack of closure for the subsets of data retained by both u_* and σ_w filters remained the same compared to the unfiltered datasets. Noticeably, I_u and I_w filters removed data from the higher end of the available energy range ($R_{nS}-G-S_v > 400 \text{ W m}^{-2}$) as shown for the pooled data in Fig. 9. The selective deletion of fluxes in this portion of the graph helps to explain the resulting increase in the OLR slopes. Significant reductions between 17 and 44 W m^{-2} in the EBR averaged over all phenophases/seasons are achieved from 1030 to 1430 h (Fig. 9). Usage of both u_* and σ_w resulted in a minor decrease in EB residual from 0730 to 0930 h only, and the difference in the residual is significant only for the 0830 h estimate for u_* (Fig. 9).

To gain insight into the atmospheric conditions that produce non-negligible advection as identified by the u_{TKE} -based criteria, we computed the stability parameter z/L and the difference in air temperature

observed between the location of the EC system (13 m above ground) and a second thermometer installed at mid-canopy (6 m above ground) for daytime data binned into half-decade u_{TKE} classes of increasing turbulence. Fig. 10 shows that under low turbulence ($u_{TKE} < 1.0 \text{ m s}^{-1}$), the periods filtered out by I_u - I_w were measured in conditions much closer to a neutral and more stratified atmosphere (larger temperature difference) when compared to periods that passed the screening, which were measured in a strongly unstable atmosphere.

The effect of the removal of advection-affected fluxes on daytime NEE was examined on a series of response curves to independent driving variables for CO_2 exchange for the growing seasons: PAR for daytime and SWC at night (Fig. 11). Data collected during the leafless and senescing canopy periods were excluded. A rectangular hyperbolic model (Eq. (23)) was fitted to each dataset:

$$NEE = -\frac{\alpha \cdot \beta \cdot \text{PAR}}{\alpha \cdot \text{PAR} + \beta} + R \quad (23)$$

Table 2

Critical values for low mixing conditions during daytime and nighttime at the Chamela site by season. The percentage of NEE data retained by each normalized turbulence indicator is shown.

Season	Filter	Critical values		Data retained (%)	
		Day	Night	Day	Night
Senescence 2007–2008	I_u	1.9	4.5	25	69
	I_w	0, 0.18	–0.17, 0.10		
	u_*	0.09	0.05	92	86
	σ_w	0.16	0.14	91	41
Leafless 2008	I_u	2.0	1.6	63	8
	I_w	–0.10, 0.24	–0.13, 0.09		
	u_*	0.12	0.09	91	56
	σ_w	0.16	0.11	92	65
Growth 2008	I_u	2.4	3.8	68	82
	I_w	–0.01, 0.23	–, 0.22		
	u_*	0.11	– ^a	89	100
	σ_w	0.15	–	90	100
Leafless 2009	I_u	2.3	3.6	69	43
	I_w	–0.17, 0.36	–0.14, 0.38		
	u_*	0.11	0.08	94	67
	σ_w	0.15	0.11	93	73
Growth 2009	I_u	2	2.5	60	59
	I_w	–0.03, 0.38	–0.23, 0.00		
	u_*	0.15	0.11	86	61
	σ_w	0.21	0.12	84	85
Senescence 2009–2010	I_u	1.9	3.3	30	64
	I_w	–0.05, 0.23	–0.27, 0.08		
	u_*	0.13	0.07	85	84
	σ_w	0.16	0.13	89	73
Growth winter rains 2010	I_u	1.9	–	45	83
	I_w	–0.04, 0.32	–, 0.07		
	u_*	0.26	0.09	75	71
	σ_w	0.25	0.12	82	72
Senescence winter rains 2010	I_u	2.3	3.6	73	49
	I_w	–0.11, 0.36	–0.43, 0.13		
	u_*	0.32	0.09	81	64
	σ_w	0.24	0.11	90	80
Growth 2010	I_u	2.3	2.8	58	58
	I_w	–0.02, 0.34	–, 0.14		
	u_*	0.09	0.13	95	50
	σ_w	0.20	–	86	100

^a No dependence of NEE on the turbulence scale could be detected, all data are kept.

where α is the apparent quantum yield ($\mu\text{mol CO}_2 \mu\text{mol photons}^{-1}$), β is the asymptotic NEE at high irradiance ($\mu\text{mol CO}_2 \text{m}^{-2} \text{s}^{-1}$) and R is the daytime ecosystem respiration ($\mu\text{mol CO}_2 \text{m}^{-2} \text{s}^{-1}$). Negative NEE indicates net photosynthesis. These parameters, found by nonlinear regression (Table 4), show confidence intervals that overlap between the filtered and unfiltered data, indicating that none of the filters changed the light response curve for daytime NEE significantly. The nighttime ecosystem respiration (R_{eco}) response to soil water availability was examined by linear regression for all datasets and the same non-significant effects were found for all filtering criteria (Table 4).

The spatial context of our flux measurements before and after the screening procedure shows that periods filtered out by I_u – I_w have a different geographical origin at daytime compared to fluxes rejected by both u_* and σ_w (Fig. 12). The portion of land that contributes mostly to fluxes discarded by the later criteria is situated in the NE quadrant, spreading in a funnel shaped pattern whose central axis lies about 30°. The effectiveness of both u_* and σ_w to filter out fluxes originated in the problematic area in the NE quadrant explains the almost exponential relationship between the wind trajectory complexity L_t and the proportion of rejected periods by u_* and σ_w alike (Fig. 14), especially at daytime. A visual inspection of the spatial pattern of L_t (Fig. 3) and the flux source area for the periods rejected by u_* and σ_w confirms that such periods did originate in difficult terrain, according to the flux footprint model. Interestingly enough, the exclusion of those periods did not improve the energy budget closure (Table 3).

Acevedo et al. (2009) have shown that the use of u_* to filter out

Table 3

Seasonal ordinary linear regression coefficients for energy balance closure after removal of data points affected by low turbulence.

Season	Filter	OLR coefficients (± SE)		
		Slope	Intercept	Adjusted r^2
Senescence ^a 2007–2008	None	0.76 ± 0.01	18.92 ± 1.45	0.83
	I_u & I_w	0.93 ± 0.01	16.47 ± 1.59	0.85
	u_*	0.76 ± 0.01	19.85 ± 1.63	0.83
Leafless 2008	σ_w	0.75 ± 0.01	23.04 ± 2.48	0.80
	None	0.75 ± 0.01	23.22 ± 1.55	0.84
	I_u & I_w	0.78 ± 0.01	38.14 ± 3.98	0.77
Growth 2008	u_*	0.74 ± 0.01	29.04 ± 2.20	0.82
	σ_w	0.74 ± 0.01	28.46 ± 2.09	0.82
	None	0.75 ± 0.01	13.53 ± 2.08	0.87
Leafless 2009	I_u & I_w	0.78 ± 0.01	10.11 ± 2.21	0.90
	u_*	0.75 ± 0.01	14.33 ± 2.18	0.87
	σ_w	0.75 ± 0.01	14.05 ± 2.21	0.87
Growth 2009	None	0.74 ± 0.00	25.81 ± 1.27	0.83
	I_u & I_w	0.82 ± 0.01	30.95 ± 1.77	0.85
	u_*	0.72 ± 0.01	31.27 ± 1.63	0.82
Senescence 2009–2010	σ_w	0.73 ± 0.01	30.04 ± 1.58	0.82
	None	0.73 ± 0.00	14.39 ± 1.21	0.84
	I_u & I_w	0.79 ± 0.01	12.22 ± 1.57	0.87
Growth winter rains 2010	u_*	0.72 ± 0.01	20.34 ± 1.68	0.82
	σ_w	0.73 ± 0.01	16.37 ± 1.42	0.84
	None	0.83 ± 0.01	16.87 ± 1.09	0.82
Senescence winter rains 2010	I_u & I_w	0.93 ± 0.01	12.11 ± 1.28	0.83
	u_*	0.83 ± 0.01	20.25 ± 1.26	0.82
	σ_w	0.82 ± 0.01	19.82 ± 1.38	0.81
Growth 2010	None	0.80 ± 0.01	17.60 ± 1.87	0.84
	I_u & I_w	0.89 ± 0.01	14.21 ± 2.05	0.87
	u_*	0.81 ± 0.01	21.45 ± 2.44	0.84
Senescence winter rains 2010	σ_w	0.80 ± 0.01	21.39 ± 2.43	0.84
	None	0.72 ± 0.01	25.13 ± 1.99	0.86
	I_u & I_w	0.78 ± 0.01	29.55 ± 2.70	0.87
Growth 2010	u_*	0.71 ± 0.01	30.53 ± 2.71	0.85
	σ_w	0.71 ± 0.01	27.23 ± 2.35	0.85
	None	0.76 ± 0.01	19.87 ± 1.44	0.83
Growth 2010	I_u & I_w	0.84 ± 0.01	18.49 ± 1.84	0.86
	u_*	0.74 ± 0.01	28.07 ± 2.02	0.81
	σ_w	0.76 ± 0.01	19.72 ± 1.54	0.84

^a Energy balance for the senescing season of 2007–2008 does not include the correction of radiant fluxes over complex topography.

periods with low turbulence intensity might not be appropriate because u_* is in itself a flux, not an independent state variable, and therefore is influenced by the scale of measurement. Whenever the turbulent exchange dominates the transport, it can be expected that the magnitude of the u_* flux does correlate with the local turbulence intensity, but there are conditions in which processes at a larger scale, the mesoscale range, dominate, and fluxes at the mesoscale range are more variable, erratic, and can be of either sign (Acevedo et al., 2009). The mesoscale exchange is largely independent of local processes, so locally calm periods can be classified as turbulent using u_* if the mesoscale transport is large enough. Conversely, buoyancy-driven turbulence may develop over complex terrain or heterogeneous surfaces under unstable conditions and low wind speeds; in such conditions, the vertical mesoscale momentum transfer may be positive, and will cancel the turbulent momentum flux, so that the measured u_* is close to zero, and the period is classified as non-turbulent even when the turbulent exchange of scalars is nonzero (Wharton et al., 2009). Acevedo et al. (2009) propose σ_w as an alternative to u_* , because σ_w is not a flux and therefore is not scale-dependent. They found that the use of σ_w for turbulence classification improved significantly their flux correction procedure, provided easier determination of the threshold, kept a larger number of data, and resulted in larger rates of respiration in the filtered dataset compared to the u_* filter. They, however, state that during calm conditions, whenever horizontal or vertical advection play a large role in the mass and energy exchange, the difficulties in assessing the total flux remain. At our site, we did not find σ_w to be a better criterion for turbulence

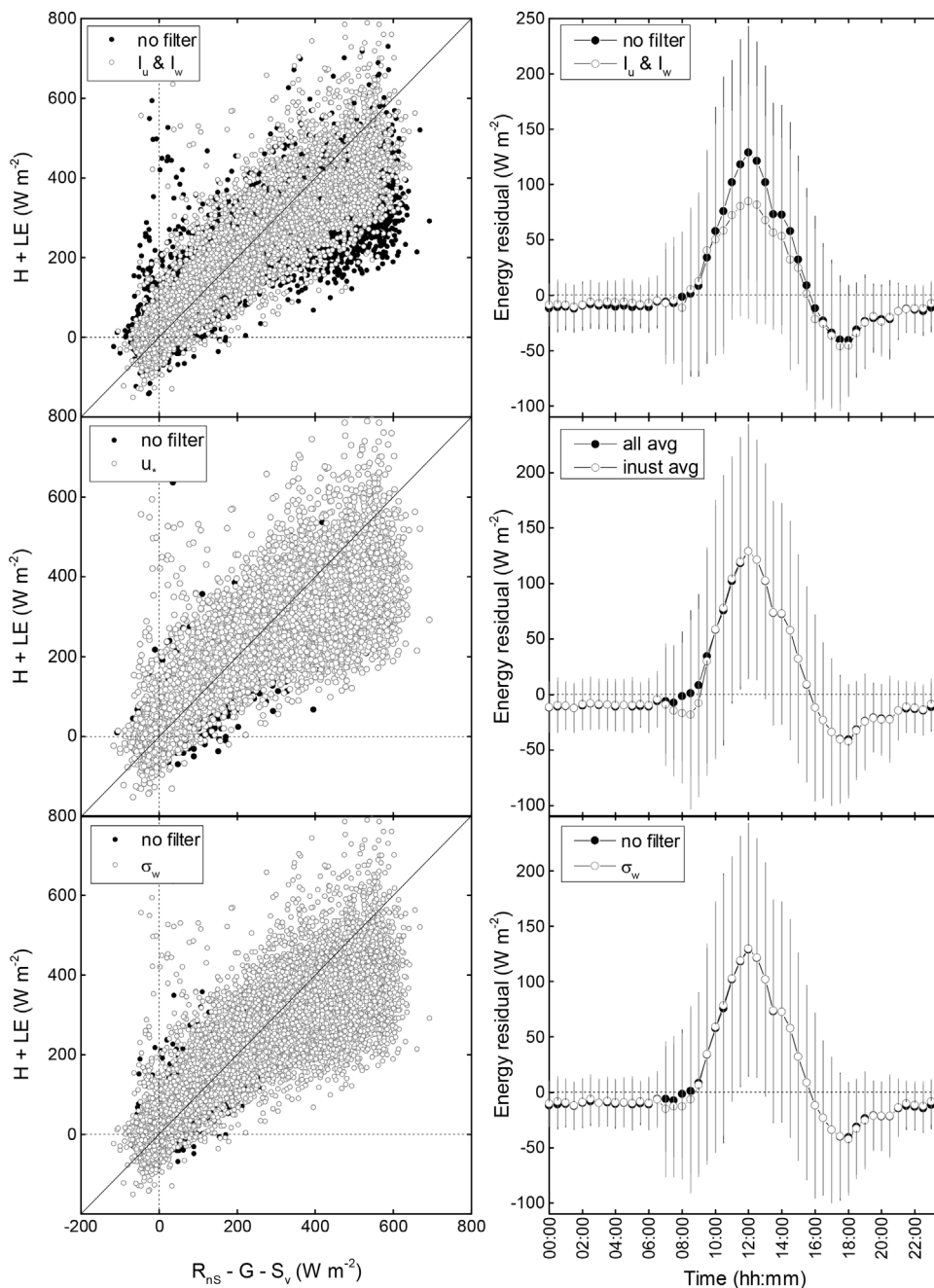


Fig. 9. Energy balance closure (left) and residual (right) for all available EC fluxes (black) and for the subset of measurements made under negligible advective conditions (white) identified by the u_{TKE} -based (top), u_* (middle) and σ_w (bottom) filters. The thin black line indicates a 1:1 relationship as reference.

classification, particularly at daytime, when I_u and I_w showed a better ability to discriminate between periods when the advective flow is relatively more important than the turbulent exchange, and therefore a substantial portion of the total flux goes undetected by the EC system. By filtering out these periods, the use of I_u - I_w consistently raised the slope of the energy balance regression for the subset of data kept by the filters. Similarly to σ_w , u_{TKE} is not a flux but a modified turbulence velocity scale, a direct measurement of the efficiency of the turbulent transport of energy and mass through the boundary layer, and the u_{TKE} -derived ratios I_u and I_w are dimensionless, simple measurements of the relative importance of advective vs. turbulent transport.

Figs. 12 and 13, show that although some periods rejected by I_u - I_w come also from the NE, it is the western sector between 230° and 310° that contributes the most to both the advection-affected and periods with well-developed turbulence. This portion of terrain is characterized by low to moderately complex topography (Fig. 3), thus no clear relationship between L_t and the proportion of filtered-out half hours exist

for the u_{TKE} -based criteria (Fig. 14). This result is contrary to our expectation that fluxes coming from the most difficult terrain might be characterized by larger I_u - I_w magnitudes and lower turbulent transport, since it is in those areas where topographically-induced drainage flow may carry away more heat or CO₂, undetected to the EC system. On this matter we conclude that the relative importance of advective flow in the periods excluded by I_u and I_w is not necessarily related to topographic features of the source area.

An explanation of the relatively poor performance of the traditionally used u_* as indicator of well-developed turbulence may lie in the characteristics of the flow in the roughness sublayer above plant canopies, that is characterized by the existence of large coherent structures (Shaw et al., 2013). Field observations and simulations show that turbulent motions and scalar transport at the interface of the canopy and the air immediately above are dominated by ramp-like patterns of downwind ejections and upstream sweeps. As the daytime buoyancy develops and the atmosphere becomes increasingly unstable, a spatial

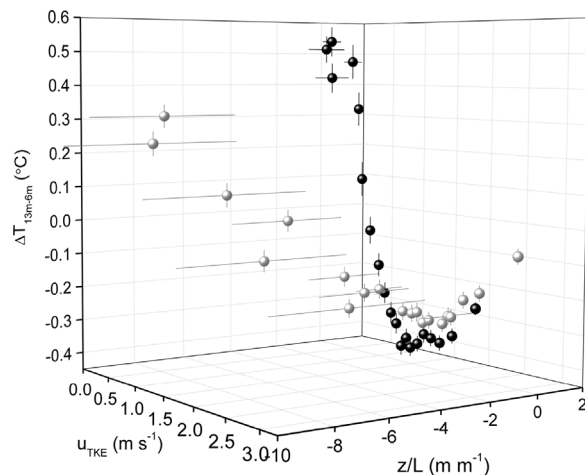


Fig. 10. Atmospheric stability (z/L) and the difference in air temperature at 13 m and 6 m above ground for data binned into 20 classes of increasing turbulence (u_{TKE}). White spheres are averages for daytime data that passed all turbulence filters while black spheres are daytime averages for periods that fell outside the u_{TKE} -based filters I_u and I_w . Error bars are 95% confidence intervals of the averages.

separation between the momentum and the scalar transport develops, and they become disassociated. Correlation coefficients between momentum and scalar transport are smaller for unstable atmospheres, the implication being that their respective transport occurs by different eddies or by different parts of the flow structures, separated both in space and time (Shaw et al., 2013). Such a decorrelation between scalar and momentum flux could explain the lack of effectiveness of u_* as indicator of scalar transport close to the canopy found in this study. The implications of these observed and simulated turbulent structures for the other two scales examined here is yet to be investigated; we can only speculate that the ability of I_u and I_w to discriminate bad periods even during daytime might indicate that these scales would not show

Table 4
Non-linear regression parameters and 95% confidence intervals for the rectangular hyperbola model fitted to unfiltered and filtered NEE at daytime, and OLS coefficients for the response of nighttime NEE (R_{eco}) to water availability in the soil.

	Filter	Parameter	Value	SE	95% LCL	95% UCL
Daytime	None	α	−0.033	0.004	−0.024	−0.041
		β	−18.68	0.55	−17.61	−19.76
		R	3.97	0.48	4.91	3.02
	I_u & I_w	α	−0.038	0.007	−0.025	−0.052
		β	−18.485	0.31	−17.16	−19.80
		R	3.79	0.69	5.14	2.44
	u_*	α	−0.037	0.006	−0.026	−0.048
		β	−18.25	0.55	−17.16	−19.34
		R	4.19	0.59	5.36	3.03
	σ_w	α	−0.038	0.006	−0.026	−0.050
		β	−17.31	0.55	−16.23	−18.40
		R	3.77	0.61	4.98	2.57
Nighttime	None	slope	29.48	2.61	23.99	34.97
		intercept	−1.16	0.40	−2.00	−0.32
	I_u & I_w	slope	28.94	2.87	22.9	34.98
		intercept	−0.81	0.46	−1.77	0.14
	u_*	slope	32.87	3.48	25.56	40.17
		intercept	−1.27	0.53	−2.39	−0.15
	σ_w	slope	31.68	2.93	25.52	37.84
		intercept	−1.15	0.45	−2.10	−0.19

the same decorrelation pattern within the roughness sublayer.

Finally, it is worth acknowledging that a most visible limitation of this study is the fact that none of the indicators of advection-prone conditions are actual measurements of advection, but only indirect indicators of its importance relative to turbulent exchange. Moreover, only wind velocity gradients developed are addressed with the use of the turbulence scales compared here, but the scalar concentration gradients surely also contribute to the advective flow and therefore to

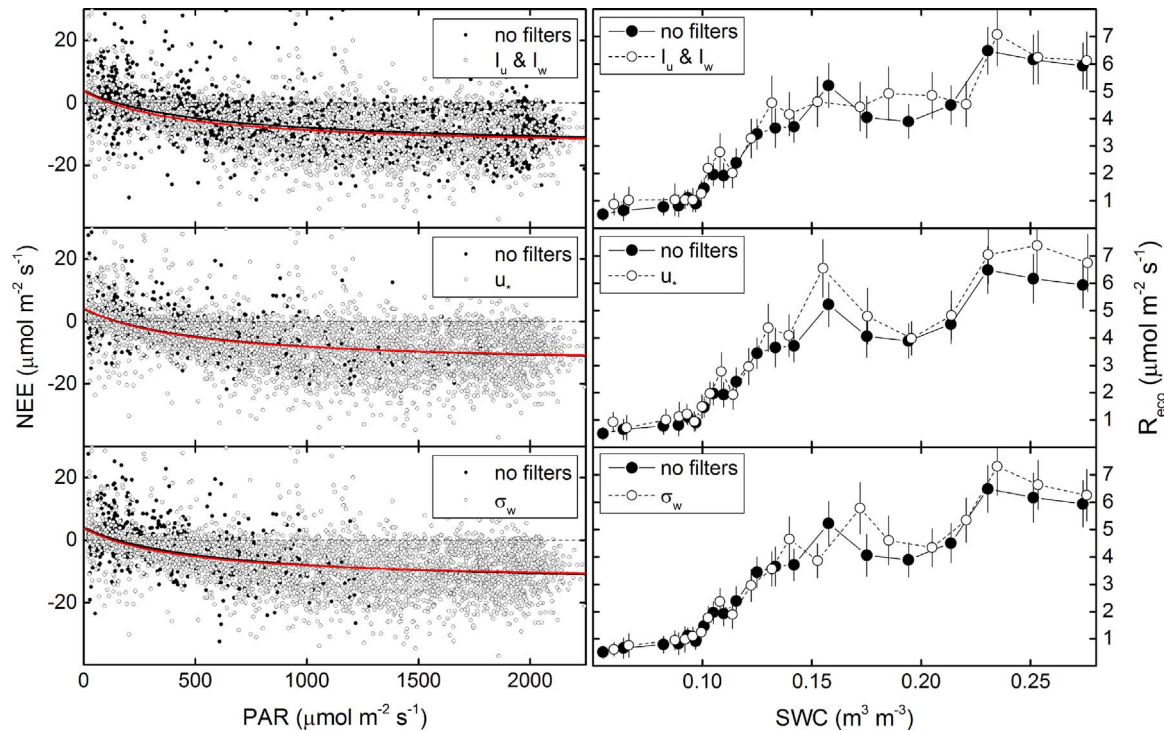


Fig. 11. Left: average response of daytime NEE to light for datasets filtered using u_{TKE} -based I_u and I_w (top), u_* (middle) and σ_w (bottom) criteria. Red and black lines are the rectangular hyperbolic light response functions for the filtered dataset and the whole dataset, respectively. Right: average response of nighttime R_{eco} to SWC for non-screened and screened data. R_{eco} were binned over 20 classes of increasing SWC. Error bars are 95% confidence intervals of the means. (For interpretation of the references to colour in this figure legend, the reader is referred to the web version of this article.)

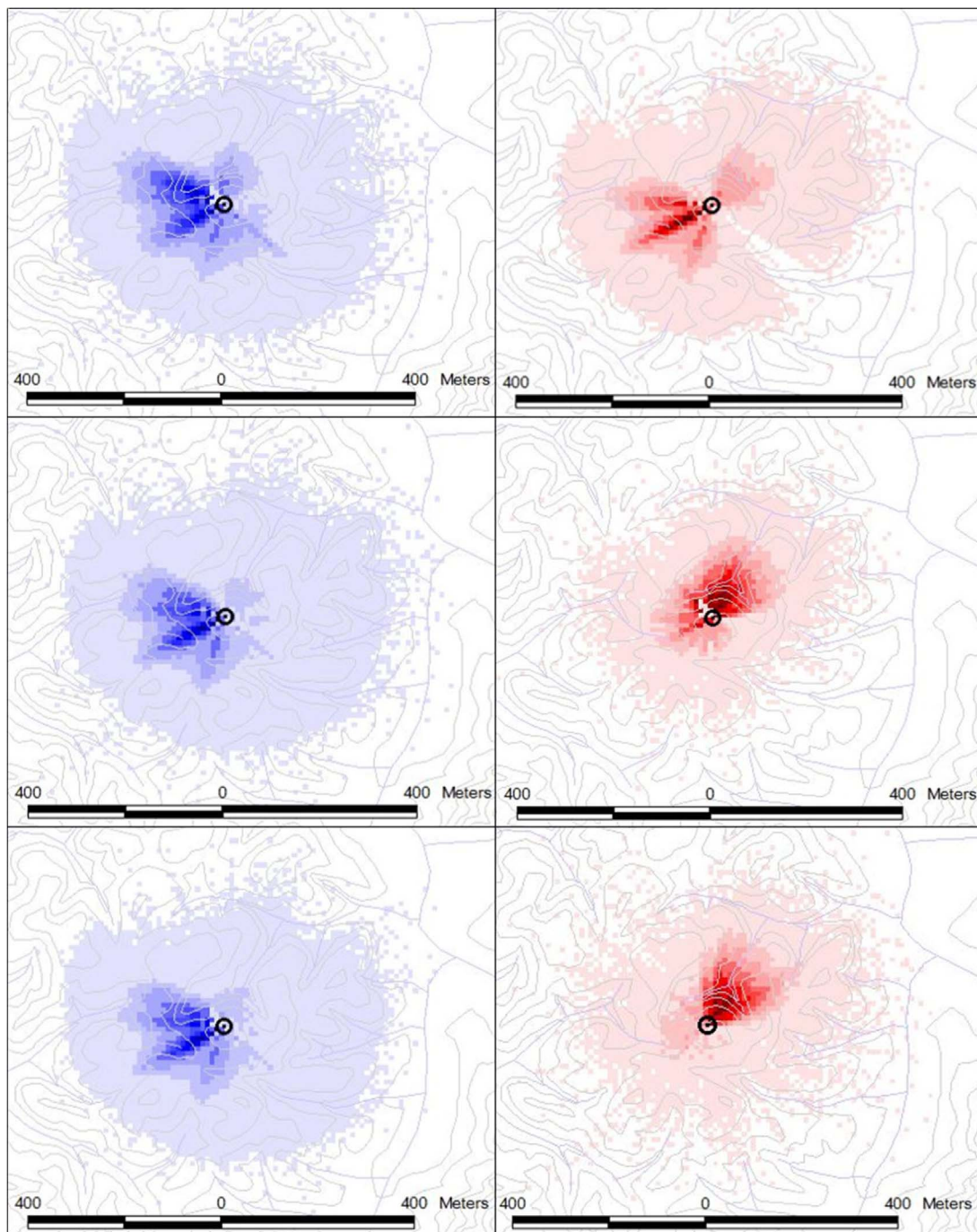


Fig. 12. Daytime sums of flux source area around the tower (black circle) for measurement periods that passed (blue) and were rejected (red) by each turbulence filter (u_{TKE} -based filters on top, u_* on middle and σ_w on bottom plots). Contributions to footprint function f^y were aggregated into 10×10 m cells and expressed as percentages (color scale) of the maximum local contribution for each dataset. Light gray curves are contour lines 10 m apart. (For interpretation of the references to colour in this figure legend, the reader is referred to the web version of this article.)

the underestimation of total exchange of carbon and energy. These gradients are an inescapable feature of complex terrain since both incident radiation and vegetation growth is naturally uneven along hill-sides, valley bottoms and hilltops, and therefore carbon, water and heat sinks and sources develop inevitably on the horizontal dimension. Along the vertical, foliage development is also uneven, and the forest floor is normally a source of CO_2 , so even over flat terrain, scalar gradients form. Additionally, there are other factors that have been proposed as causes for the general lack of EB closure in all flux studies that are not related to advection, that were not addressed in this investigation, and that likely still play a role. We used the EBC as an

indicator of flux quality but the effect of such other factors must be kept in mind when interpreting the results of any filtering or correction scheme on fluxes.

4. Conclusions

We demonstrate that it is possible to measure carbon dioxide, latent and sensible heat fluxes over a tropical dry forest situated in moderately complex terrain using the eddy covariance technique. The implementation of three procedures produced a reduced dataset of quality comparable to those obtained in more ideal conditions. The available

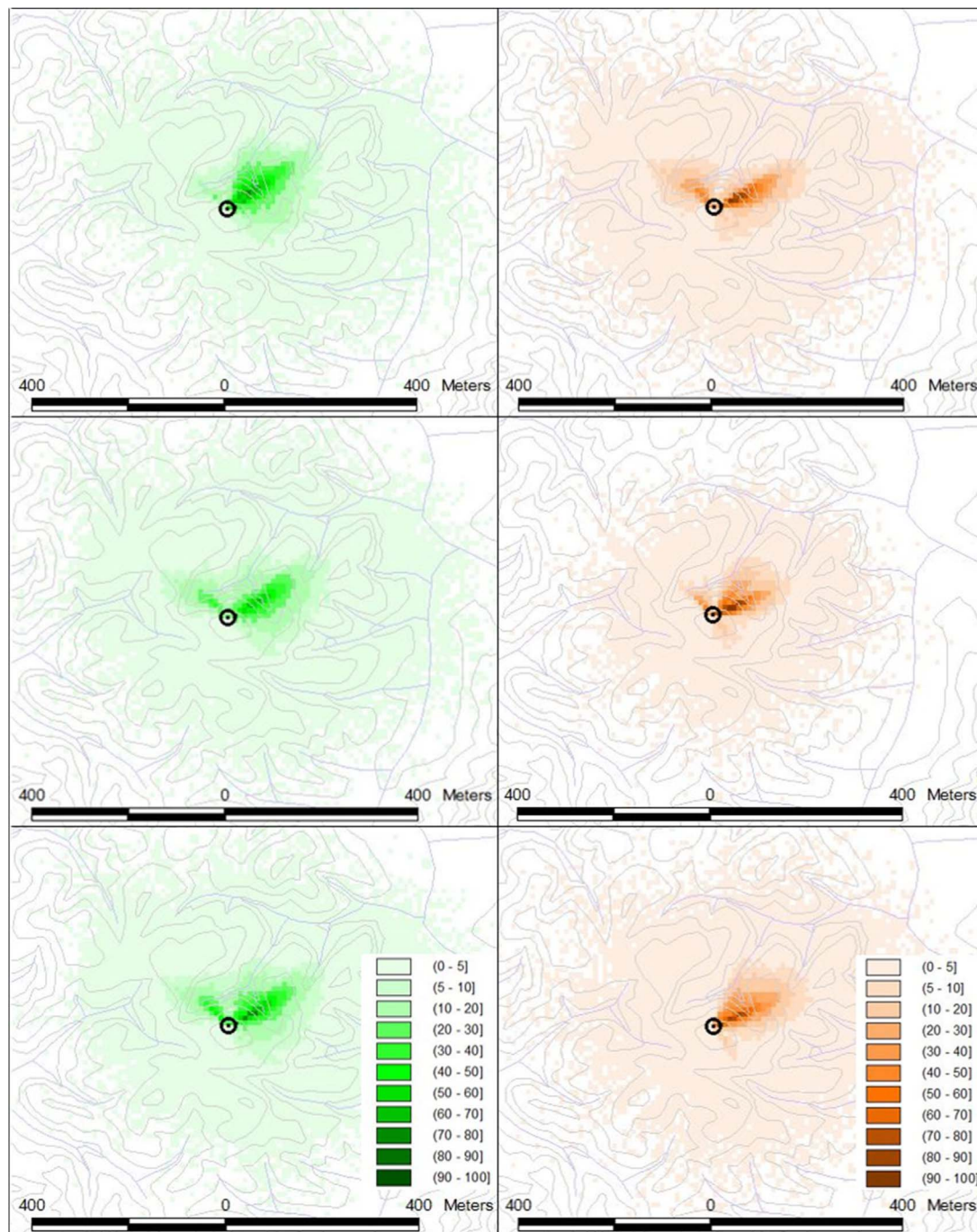


Fig. 13. Same as Fig. 11, but for nighttime. Flux footprint for periods that passed the turbulence test is in green, while that of rejected periods is in orange. (For interpretation of the references to colour in this figure legend, the reader is referred to the web version of this article.)

incoming radiation was modeled considering the aspect and slope of the surface, and in general resulted in a reduced amount of available energy, and therefore in a higher energy balance closure. Additionally, the use of even crude estimates of the energy stored in the air and the canopy below the net radiation measurement height incorporated to the energy budget a portion of the thermal energy that often goes unaccounted for. Finally, the use of dimensionless filters that are inversely proportional to the effectiveness of the turbulent transport of mass and energy were effective to discriminate and eliminate periods when the vertical or horizontal advection cannot be neglected.

The findings of this work may be widely applicable to EC measurements over both simple but non-flat terrain, as well as more complex topography. The corrections applied to the net radiation and the

use of the u_{TKE} filters require only quantities already measured in most flux study sites. The establishment of new field sites for EC measurements should always seek to comply with the assumptions of the theory behind and look for flat, homogeneously covered terrain, which greatly simplifies the estimation of total flux of scalars, but given the fact that some vegetation types such as tropical dry forests are now largely confined to non-ideal conditions for EC measurements, a thoughtful application of the tools described here can produce a dataset of quality comparable to those of more ideal conditions. Along with the usage of remote sensing products, better measurements of vegetation energy storage, and biometric estimates of carbon stored and released, these quality control procedures may aid in the assessment of the dynamics of carbon and energy fluxes in systems that are often ignored in global

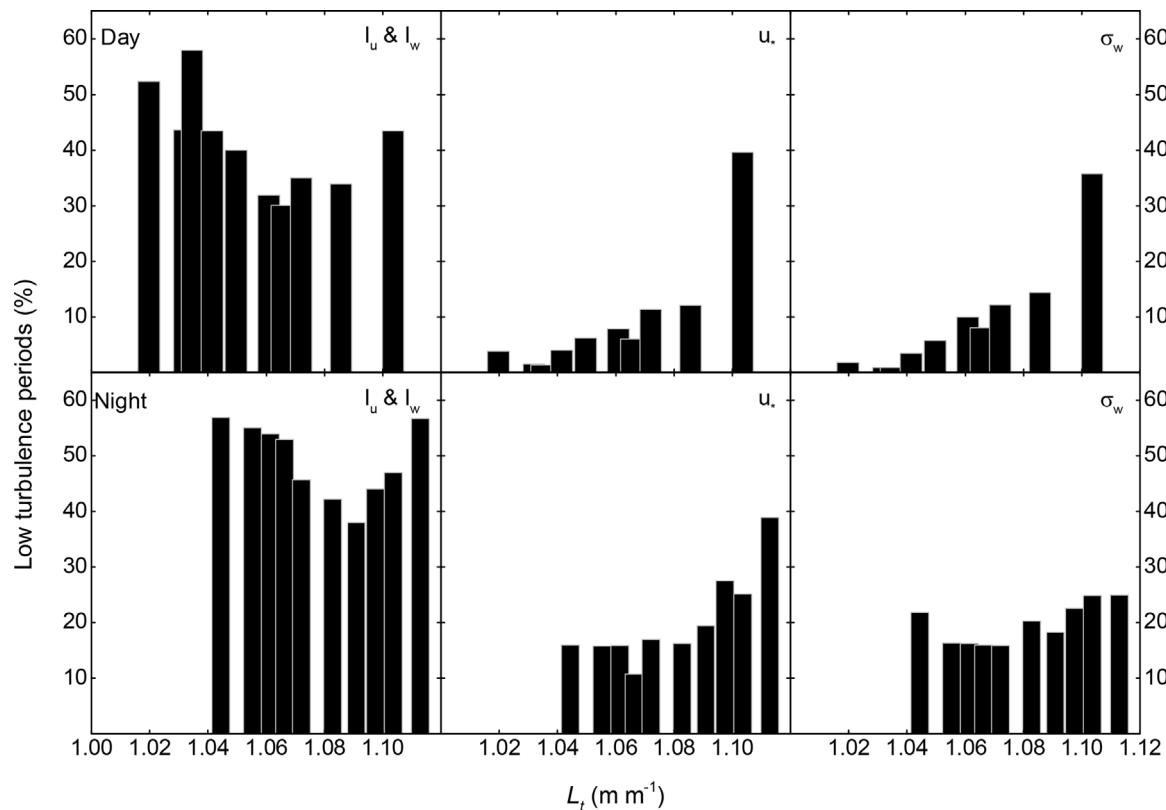


Fig. 14. Percentage of half hour periods flagged as affected by advection by each turbulence scale at daytime (top) and nighttime (bottom) in relation to L_t , a measurement of terrain complexity for the wind trajectory. Bars are centered on the median of each L_t decile.

models of primary productivity and atmosphere-surface interactions.

Acknowledgments

This work was supported by the Inter-American Institute for Global Change Research (IAI), grants CRNII and CRNIII 21, and a CONACyT-UCMEXUS scholarship (175725) to EGC. We gratefully thank the support of the staff at the Estación de Biología Chamela (UNAM), and the field and laboratory assistance of Jorge Vega, Abel Verduzco, Irais Medina, Jesús Oliván and Diego Flores (UNAM), and Peter Carlson and Mei-Mei Chong (University of Alberta). We are grateful to two anonymous reviewers that provided comments and questions that greatly improved the quality of this manuscript.

References

- Acevedo, O.C., Moraes, O.L.L., Degrazia, G.A., Fitzjarrald, D.R., Manzi, A.O., Campos, J.G., 2009. Is friction velocity the most appropriate scale for correcting nocturnal carbon dioxide fluxes? *Agric. For. Meteorol.* 149, 1–10.
- Aubinet, M., Grelle, A., Ibrom, A., Rannik, U., Moncrieff, J., Foken, T., Kowalski, A.S., Martin, P.H., Bernigier, P., Bernhofer, C., Clement, R., Elbergs, J., Granier, A., Grünwald, T., Morgenstern, K., Pilegaard, K., Rebmann, C., Snijders, W., Valentini, R., Vesala, T., 2000. Estimates of the annual net carbon and water exchange of forests: the EUROFLUX methodology. *Adv. Ecol. Res.* 30, 113–175.
- Barcza, Z., Kern, A., Haszpra, L., Kljun, N., 2009. Spatial representativeness of tall tower eddy covariance measurements using remote sensing and footprint analysis. *Agric. For. Meteorol.* 149, 795–807.
- Barr, A.G., Morgenstern, K., Black, T.A., McCaughey, J.H., Nesic, Z., 2006. Surface energy balance closure by the eddy-covariance method above three boreal forest stands and implications for the measurement of CO_2 flux. *Agric. For. Meteorol.* 140, 322–337.
- Ceballos, G., Garcia, A., 1995. Conserving Neotropical diversity: the role of dry forests in western Mexico. *Conserv. Biol.* 9, 1349–1356.
- Cotler, H., Durán, E., Siebe, C., 2002. Caracterización morfoedafológica y calidad de sitio de un bosque tropical caducifolio. In: Noguera, F.A., Vega-Rivera, J., García-Aldrete, A.N., Quesada-Avenida, M. (Eds.), *Historia Natural de Chamela*. Instituto de Biología, UNAM, Mexico, pp. 17–79.
- Duffie, J.A., Beckman, W.A., 2006. *Solar Engineering of Thermal Processes*, 3rd. ed. John Wiley and Sons, Hoboken, New Jersey.
- Erbs, D.G., Klein, S.A., Duffie, J.A., 1982. Estimation of the diffuse radiation fraction for hourly, daily and monthly-average global radiation. *Sol. Energy* 28, 293–302.
- García, E., 1988. *Modificaciones al Sistema de Clasificación Climática de Köppen* (para adaptarlo a las condiciones de la República Mexicana), 4th ed. UNAM, Mexico City, Mexico.
- Goulden, M.L., Munger, W.J., Fan, S.M., Daule, B.C., Wofsy, S., 1996. Measurements of carbon sequestration by long-term eddy covariance: methods and a critical evaluation of accuracy. *Glob. Change Biol.* 2, 69–182.
- Gu, L.H., Falge, E.M., Boden, T., Baldocchi, D.D., Black, T.A., Saleska, S.R., Suni, T., Verma, S.B., Vesala, T., Wofsy, S.C., Xu, L.K., 2005. Objective threshold determination for nighttime eddy flux filtering. *Agric. For. Meteorol.* 128, 179–197.
- Haslwanter, A., Hammerle, A., Wohlfahrt, G., 2009. Open-path vs. closed-path eddy covariance measurements of the net ecosystem carbon dioxide and water vapour exchange: a long-term perspective. *Agric. For. Meteorol.* 149, 291–302.
- Hay, J.H., 1993. Calculating solar radiation for inclined surfaces: practical approaches. *Renew. Energy* 3, 373–380.
- Hollinger, D.Y., Kelliher, F.M., Byers, J.N., Hunt, J.E., McSeveny, T.M., Weir, P.L., 1994. Carbon dioxide exchange between an undisturbed old-growth temperate forest and the atmosphere. *Ecology* 75, 134–150.
- Holst, T., Rost, J., Mayer, H., 2005. Net radiation balance for two forested slopes on opposite sides of a valley. *Int. J. Biometeorol.* 49, 275–284.
- Hopkinson, C., Chasmer, L., Barr, A.G., Kljun, N., Black, T.A., McCaughey, J.H., 2016. Monitoring boreal forest biomass and carbon storage change by integrating airborne laser scanning, biometry and eddy covariance data. *Remote Sens. Environ.* 181, 82–95.
- Jaramillo, V.J., Kauffmann, J.B., Renteria-Rodriguez, L., Cummings, D.L., Ellingson, L.J., 2003. Biomass, Carbon and Nitrogen pools in Mexican tropical dry forest landscapes. *Ecosystems* 6, 609–629.
- Kauffman, J.B., Steele, M.D., Cummings, D.L., Jaramillo, V.J., 2003. Biomass dynamics associated with deforestation, fire, and conversion to cattle pasture in a Mexican tropical dry forest. *For. Ecol. Manage.* 176, 1–12.
- Kljun, N., Calanca, P., Rotach, M.W., Schmid, H.P., 2004. A simple parameterization for flux footprint predictions. *Boundary-Layer Meteorol.* 112, 503–523.
- Kochendorfer, J., Castillo, E.G., Haas, E., Oechel, W.C., 2011. Net ecosystem exchange, evapotranspiration and canopy conductance in a riparian forest. *Agric. For. Meteorol.* 151, 544–553.
- Leuning, R., van Gorsel, E., Massman, W.J., Isaac, P.R., 2012. Reflections on the surface energy imbalance problem. *Agric. For. Meteorol.* 156, 65–74.
- Liu, B.Y.H., Jordan, R.C., 1962. Daily insolation on surfaces tilted towards the equator. *ASHRAE Trans.* 67, 526–541.
- Magaña, V.O., Vázquez, J.L., Pérez, J.B., 2003. Impact of El Niño on precipitation in Mexico. *Geofísica Int.* 42, 313–330.
- Mahli, Y., Nobre, A.D., Grace, J., Kruijt, B., Pereira, M.G., Culf, A., Scott, S., 1998. Carbon

- dioxide transfer over a Central Amazonian rain forest. *J. Geophys. Res.-Atmos.* 103, 31593–31612.
- Martinez-Yrizar, A., Sarukhan, J., Perez-Jimenez, A., Rincon, E., Maass, J.M., Solis-Magallanes, A., Cervantes, L., 1992. Above-ground phytomass of a tropical deciduous forest on the coast of Jalisco, Mexico. *J. Trop. Ecol.* 8, 89–96.
- Martinez-Yrizar, A., Maass, J.M., Pérez-Jiménez, L.A., Sarukhán, J., 1996. Net primary productivity of a tropical deciduous forest ecosystem in western Mexico. *J. Trop. Ecol.* 12, 169–175.
- Massman, W.J., 2000. A simple method for estimating frequency response corrections for eddy covariance systems. *Agric. For. Meteorol.* 104, 185–198.
- Matzinger, N., Andretta, M., van Gorsel, E., Vogt, R., Ohmura, A., Rotach, M.W., 2003. Surface radiation budget in an Alpine valley. *Q. J. R. Meteorol. Soc.* 129, 877–895.
- McCaughey, J.H., Saxton, W.L., 1988. Energy balance storage terms in a mixed forest. *Agric. For. Meteorol.* 44, 1–18.
- Meeus, J.A., 1998. *Astronomical Algorithms*, 2nd. ed. Willmann-Bell Inc., Richmond, VA.
- Mooney, H.A., Bullock, S.H., Medina, E., 1995. Introduction. In: Bullock, S.H., Mooney, H.A., Medina, E. (Eds.), *Seasonally Dry Tropical Forests*. Cambridge University Press, Cambridge, pp. 1–8.
- NOAA Climate Prediction Center, 2016. Cold and Warm Episodes by Season. http://origin.cpc.ncep.noaa.gov/products/analysis_monitoring/ensostuff/ONI_v5.php (Accessed 15.11.2016).
- NOAA ESRL, 2016. Solar calculation details spreadsheet. https://www.esrl.noaa.gov/gmd/grad/solcalc/NOAA_Solar_Calculations_day.xls (Accessed 4.09.2016).
- Oliphant, A.J., Grimmond, C.S.B., Zutter, H.N., Schmid, H.P., Su, H.B., Scott, S.L., Offerle, B., Randolph, J.C., Ehman, J., 2004. Heat storage and energy balance fluxes for a temperate deciduous forest. *Agric. For. Meteorol.* 126, 185–201.
- Ono, K., Mano, M., Miyata, A., Inoue, Y., 2008. Applicability of the planar fit technique in estimating surface fluxes over flat terrain using eddy covariance. *J. Agric. Meteorol.* 64, 121–130.
- Pérez-Ruiz, E.R., Garatuza-Payán, J., Watts, C.J., Rodríguez, J.C., Yépez, E.A., Scott, R.L., 2010. Carbon dioxide and water vapour exchange in a tropical dry forest as influenced by the North American Monsoon System (NAMS). *J. Arid Environ.* 74, 556–563.
- Park, Y.S., Paw U, K.T., 2004. Numerical estimations of horizontal advection inside canopies. *J. Appl. Meteorol.* 43, 1530–1538.
- Paw U, K.T., Baldocchi, D.D., Meyers, T.P., Wilson, K.B., 2000. Correction of eddy-covariance measurements incorporating both advective effects and density fluxes. *Bound. Layer Meteorol.* 97, 487–511.
- Perez, R., Seals, R., Ineichen, P., Stewart, R., Menicucci, D., 1987. A new simplified version of the Perez diffuse irradiance model for tilted surfaces. *Sol. Energy* 39, 221–231.
- Portillo-Quintero, C.A., Sanchez-Azofeifa, G.A., 2010. Extent and conservation of tropical dry forests in the Americas. *Biol. Conserv.* 143, 144–155.
- Sánchez-Azofeifa, G.A., Quesada, M., Rodríguez, J.P., Nassar, J.M., Stoner, K.E., Castillo, A., Garvin, T., Zent, E.L., Calvo-Alvarado, J.C., Kalacska, M.E.R., Fajardo, L., Gamon, J.A., Cuevas-Reyes, P., 2005. Research priorities for neotropical dry forests. *Biotropica* 37, 477–485.
- Saleska, S.R., et al., 2003. Carbon in Amazon forests: unexpected seasonal fluxes and disturbance-induced losses. *Science* 302, 1554–1557.
- Samson, R., Lemeur, R., 2001. Energy balance storage terms and big-leaf evapotranspiration in a mixed deciduous forest. *Ann. For. Sci.* 58, 529–541.
- Schotanus, P., Nieuwstadt, F.T.M., DeBruin, H.A.R., 1983. Temperature measurement with a sonic anemometer and its application to heat and moisture fluctuations. *Bound. Layer Meteorol.* 26, 81–93.
- Shaw, R.H., Patton, E.G., Finnigan, J.J., 2013. Coherent eddy structures over plant canopies. In: Venditti, J.G., Best, J.L., Church, M., Hardy, R.J. (Eds.), *Coherent Flow Structures at Earth's Surface*. John Wiley & Sons Ltd., New York, pp. 149–159.
- Su, H.B., Schmid, H.P., Grimmond, C.S.B., Vogel, C.S., Oliphant, A.J., 2004. Spectral characteristics and correction of long-term eddy covariance measurements over two mixed hardwood forests in non-flat terrain. *Bound. Layer Meteorol.* 110, 213–253.
- Temps, R.C., Coulson, K.L., 1977. Solar radiation incident upon slopes of different orientations. *Sol. Energy* 19, 179–189.
- Thom, A.S., 1975. Momentum, mass and heat exchange of plant communities. In: Monteith, J.L. (Ed.), *Vegetation and the Atmosphere*, vol. 1. Academic Press, New York, pp. 57–109.
- Trejo, I., Dirzo, R., 2000. Deforestation of seasonally dry tropical forests: a national and local analysis in Mexico. *Biol. Conserv.* 94, 133–142.
- Turnipseed, A.A., Blanken, P.D., Anderson, D.E., Monson, R.K., 2002. Energy budget above a high-elevation subalpine forest in complex topography. *Agric. For. Meteorol.* 110, 177–201.
- van Gorsel, E., Berni, J.A.J., Briggs, P., Cabello-Leblic, A., Chasmer, L., Cleugh, H.A., Hacker, J., Hantson, S., Haverd, V., Hughes, D., Hopkinson, C., Keith, H., Kljun, N., Leuning, R., 2013. Primary and secondary effects of climate variability on net ecosystem carbon exchange in an evergreen Eucalyptus forest. *Agric. For. Meteorol.* 182–183, 248–253.
- Verduzco, V.S., Garatuza-Payán, J., Yépez, E.A., Watts, C.J., Rodríguez, J.C., Robles-Morua, A., Vivoni, E.R., 2015. Variations of net ecosystem production due to seasonal precipitation differences in a tropical dry forest of northwest Mexico. *J. Geophys. Res. Biogeosci.* 120, 2081–2094.
- Webb, E.K., Pearman, G.I., Leuning, R., 1980. Correction of flux measurements for density effects due to heat and water vapour transfer. *Q. J. R. Meteorol. Soc.* 106, 85–100.
- Wharton, S., Schroeder, M., Paw U, K.T., Falk, M., Bible, K., 2009. Turbulence considerations for comparing ecosystem exchange over old-growth and clear-cut stands for limited fetch and complex canopy flow conditions. *Agric. For. Meteorol.* 149, 1477–1490.
- Whiteman, C.D., Allwine, K.J., Fritschen, L.J., Orgill, M.M., Simpson, J.R., 1989. Deep valley radiation and surface energy budget microclimates. Part I: radiation. *J. Appl. Meteorol.* 28, 414–426.
- Wilczak, J.M., Oncley, S.P., Stage, S.A., 2001. Sonic anemometer tilt correction algorithms. *Bound. Layer Meteorol.* 99, 127–150.
- Wilson, K., Goldstein, A., Falge, E., Aubinet, M., Baldocchi, D., Berbigier, P., Bernhofer, C., Ceulemans, R., Dolman, H., Field, C., Grelle, A., Ibrom, A., Law, B.E., Kowalski, A., Meyers, T., Moncrieff, J., Monson, R., Oechel, W., Tenhunen, J., Valentini, R., Verma, S., 2002. Energy balance closure at FLUXNET sites. *Agric. For. Meteorol.* 113, 223–243.
- Younes, S., Claywell, R., Muneer, T., 2005. Quality control of solar radiation data: present status and proposed new approaches. *Energy* 30, 1533–1549.
- Yuan, R., Kang, M., Park, S., Hong, J., Lee, D., Joon, K., 2011. Expansion of the planar-fit method to estimate flux over complex terrain. *Meteorol. Atmos. Phys.* 110, 123–133.